

RD-A123 577

INTERPLANETARY MAGNETIC FIELD AND TROPOSPHERIC  
CIRCULATION(U) STANFORD UNIV CA INST FOR PLASMA  
RESEARCH J M WILCOX ET AL. OCT 82 SUIPR-945

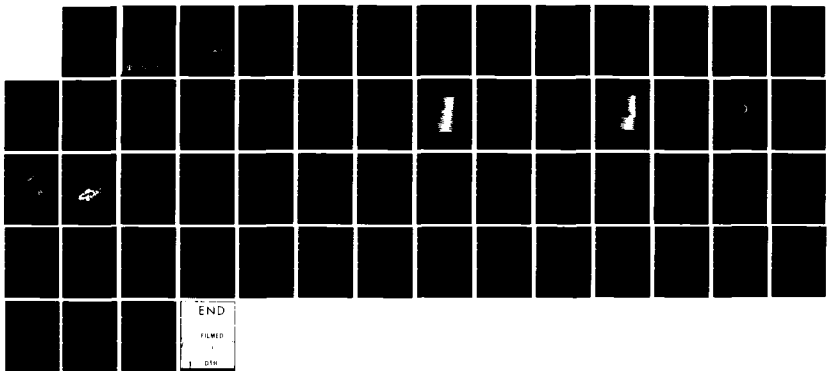
1/1

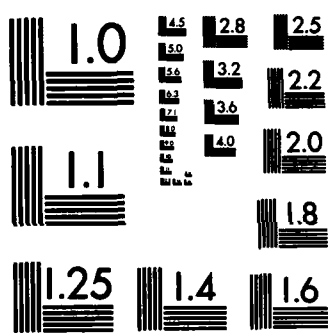
UNCLASSIFIED

N00014-76-C-0287

F/G 8/14

NL





MICROCOPY RESOLUTION TEST CHART  
NATIONAL BUREAU OF STANDARDS-1963-A

2  
2  
5  
3  
5  
2  
3  
1  
A  
D  
A

1  
*Calc 1-7  
NA 322-007*  
**INTERPLANETARY MAGNETIC FIELD  
AND TROPOSPHERIC CIRCULATION**

By

**John M. Wilcox, Philip H. Scherrer  
and J. Todd Hoeksema**

Office of Naval Research  
Contract N00014-76-C-0207

National Aeronautics and Space Administration  
Grant NGR 05-020-559 and Contract NAS5-24420

National Science Foundation  
Grant ATM77-20580

Max C. Fleischmann Foundation

SUIPR Report No. 945

October 1982

This document has been approved  
for public release and sale; its  
distribution is unlimited.

DTIC  
ELECTED  
DEC 21 1982  
S E

DTIC COPY



**INSTITUTE FOR PLASMA RESEARCH  
STANFORD UNIVERSITY, STANFORD, CALIFORNIA**

82 12 21 022

INTERPLANETARY MAGNETIC FIELD AND TROPOSPHERIC CIRCULATION

By

John M. Wilcox, Philip H. Scherrer & J. Todd Hoeksema

Office of Naval Research  
Contract N00014-76-C-0207

National Aeronautics and Space Administration  
Grant NGR 05-020-559 and Contract NAS5-24420

National Science Foundation  
Grant ATM77-20580

Max C. Fleischmann Foundation

SUIPR Report No. 945

October 1982

Accession For																																																																																																																																																																																																																																																																																																																																																																																																																																																																																																																																																																																																																																																																																																																																																																																																																																																																																																																																																																																																																																							
NTIS GRA&I <input checked="" type="checkbox"/>																																																																																																																																																																																																																																																																																																																																																																																																																																																																																																																																																																																																																																																																																																																																																																																																																																																																																																																																																																																																																																							
DOD T&E <input type="checkbox"/>																																																																																																																																																																																																																																																																																																																																																																																																																																																																																																																																																																																																																																																																																																																																																																																																																																																																																																																																																																																																																																							
Unpublished <input type="checkbox"/>																																																																																																																																																																																																																																																																																																																																																																																																																																																																																																																																																																																																																																																																																																																																																																																																																																																																																																																																																																																																																																							
Classification <i>Not on file</i>																																																																																																																																																																																																																																																																																																																																																																																																																																																																																																																																																																																																																																																																																																																																																																																																																																																																																																																																																																																																																																							
Distribution/																																																																																																																																																																																																																																																																																																																																																																																																																																																																																																																																																																																																																																																																																																																																																																																																																																																																																																																																																																																																																																							
Availability Codes																																																																																																																																																																																																																																																																																																																																																																																																																																																																																																																																																																																																																																																																																																																																																																																																																																																																																																																																																																																																																																							
1	2	3	4	5	6	7	8	9	10	11	12	13	14	15	16	17	18	19	20	21	22	23	24	25	26	27	28	29	30	31	32	33	34	35	36	37	38	39	40	41	42	43	44	45	46	47	48	49	50	51	52	53	54	55	56	57	58	59	60	61	62	63	64	65	66	67	68	69	70	71	72	73	74	75	76	77	78	79	80	81	82	83	84	85	86	87	88	89	90	91	92	93	94	95	96	97	98	99	100	101	102	103	104	105	106	107	108	109	110	111	112	113	114	115	116	117	118	119	120	121	122	123	124	125	126	127	128	129	130	131	132	133	134	135	136	137	138	139	140	141	142	143	144	145	146	147	148	149	150	151	152	153	154	155	156	157	158	159	160	161	162	163	164	165	166	167	168	169	170	171	172	173	174	175	176	177	178	179	180	181	182	183	184	185	186	187	188	189	190	191	192	193	194	195	196	197	198	199	200	201	202	203	204	205	206	207	208	209	210	211	212	213	214	215	216	217	218	219	220	221	222	223	224	225	226	227	228	229	230	231	232	233	234	235	236	237	238	239	240	241	242	243	244	245	246	247	248	249	250	251	252	253	254	255	256	257	258	259	260	261	262	263	264	265	266	267	268	269	270	271	272	273	274	275	276	277	278	279	280	281	282	283	284	285	286	287	288	289	290	291	292	293	294	295	296	297	298	299	300	301	302	303	304	305	306	307	308	309	310	311	312	313	314	315	316	317	318	319	320	321	322	323	324	325	326	327	328	329	330	331	332	333	334	335	336	337	338	339	340	341	342	343	344	345	346	347	348	349	350	351	352	353	354	355	356	357	358	359	360	361	362	363	364	365	366	367	368	369	370	371	372	373	374	375	376	377	378	379	380	381	382	383	384	385	386	387	388	389	390	391	392	393	394	395	396	397	398	399	400	401	402	403	404	405	406	407	408	409	410	411	412	413	414	415	416	417	418	419	420	421	422	423	424	425	426	427	428	429	430	431	432	433	434	435	436	437	438	439	440	441	442	443	444	445	446	447	448	449	450	451	452	453	454	455	456	457	458	459	460	461	462	463	464	465	466	467	468	469	470	471	472	473	474	475	476	477	478	479	480	481	482	483	484	485	486	487	488	489	490	491	492	493	494	495	496	497	498	499	500	501	502	503	504	505	506	507	508	509	510	511	512	513	514	515	516	517	518	519	520	521	522	523	524	525	526	527	528	529	530	531	532	533	534	535	536	537	538	539	540	541	542	543	544	545	546	547	548	549	550	551	552	553	554	555	556	557	558	559	560	561	562	563	564	565	566	567	568	569	570	571	572	573	574	575	576	577	578	579	580	581	582	583	584	585	586	587	588	589	590	591	592	593	594	595	596	597	598	599	600	601	602	603	604	605	606	607	608	609	610	611	612	613	614	615	616	617	618	619	620	621	622	623	624	625	626	627	628	629	630	631	632	633	634	635	636	637	638	639	640	641	642	643	644	645	646	647	648	649	650	651	652	653	654	655	656	657	658	659	660	661	662	663	664	665	666	667	668	669	670	671	672	673	674	675	676	677	678	679	680	681	682	683	684	685	686	687	688	689	690	691	692	693	694	695	696	697	698	699	700	701	702	703	704	705	706	707	708	709	710	711	712	713	714	715	716	717	718	719	720	721	722	723	724	725	726	727	728	729	730	731	732	733	734	735	736	737	738	739	740	741	742	743	744	745	746	747	748	749	750	751	752	753	754	755	756	757	758	759	760	761	762	763	764	765	766	767	768	769	770	771	772	773	774	775	776	777	778	779	780	781	782	783	784	785	786	787	788	789	790	791	792	793	794	795	796	797	798	799	800	801	802	803	804	805	806	807	808	809	810	811	812	813	814	815	816	817	818	819	820	821	822	823	824	825	826	827	828	829	830	831	832	833	834	835	836	837	838	839	840	841	842	843	844	845	846	847	848	849	850	851	852	853	854	855	856	857	858	859	860	861	862	863	864	865	866	867	868	869	870	871	872	873	874	875	876	877	878	879	880	881	882	883	884	885	886	887	888	889	890	891	892	893	894	895	896	897	898	899	900	901	902	903	904	905	906	907	908	909	910	911	912	913	914	915	916	917	918	919	920	921	922	923	924	925	926	927	928	929	930	931	932	933	934	935	936	937	938	939	940	941	942	943	944	945	946	947	948	949	950	951	952	953	954	955	956	957	958	959	960	961	962	963	964	965	966	967	968	969	970	971	972	973	974	975	976	977	978	979	980	981	982	983	984	985	986	987	988	989	990	991	992	993	994	995	996	997	998	999	1000

1000

INTERPLANETARY MAGNETIC FIELD AND TROPOSPHERIC CIRCULATION

John M. Wilcox, Philip H. Scherrer and J. Todd Hoeksema

Institute for Plasma Research  
Stanford University  
Stanford, California, U.S.A.

Office of Naval Research  
Contract N00014-76-C-0207

National Aeronautics & Space Administration  
Grant NGR 05-020-559 & Contract NAS5-24420

National Science Foundation  
Grant ATM77-20580

Max C. Fleischmann Foundation

SUIPR Report No. 945

October 1982

Presented at: Second International Symposium, Solar-Terrestrial  
Influences on Weather and Climate,  
Boulder, Colorado - August 1982.

# INTERPLANETARY MAGNETIC FIELD AND TROPOSPHERIC CIRCULATION

John M. Wilcox, Philip H. Scherrer and J. Todd Hoeksema

Institute for Plasma Research, Stanford University

Stanford, California

## ABSTRACT

The relation between interplanetary magnetic sector boundary crossings and areas of high vorticity in the troposphere that was reported during 1963-1973 cannot be investigated in the years after 1973 because of changes in the processing of the 500 mb height grids prepared by the National Meteorological Center. In particular, we cannot say that the effect disappeared.

The same applies to vorticity computed from NMC winds grids.

The Limited Area Fine Mesh grid has a large noise in computed vorticity after December 3, 1974. Therefore the interesting analysis of Larsen and Kelley cannot be extended. They had found that forecasts of Vorticity Area Index were significantly poorer after a sector boundary.

7

## 1. INTRODUCTION

We have reported (Wilcox, et al. 1973) that an index that measures the area of intense circulation in the wintertime northern hemisphere has a minimum value about one day after the solar wind has carried an interplanetary sector boundary past the earth. This Vorticity Area Index (VAI) was defined by Roberts and Olson (1973) as the area within the vorticity contours of  $20 \times 10^{-5} \text{ s}^{-1}$  plus the area within contours of 24 of the same units. The second contour level was added to increase the influence of the regions of most intense circulation. The absolute vorticity was computed from the National Meteorological Center 500 mb height grids for the northern hemisphere north of 20 degrees N, using a simple five-point height difference computation. These grids were archived by the National Center for Atmospheric Research in Boulder.

This minimum in the VAI was discovered following 54 sector boundaries during the winter months November-March of 1964-1970 (Wilcox et al. 1974). A later analysis (Wilcox et al. 1976) using 131 boundaries in the winters 1963-1973 found a similar minimum, as shown in Figure 1. Hines and Halevy (1975, 1977) extensively analyzed our reports and made the following statement: "In reaching our initial decision to accept the alleged solar signal as a physically meaningful signal and in holding to that decision we are not asserting that physical reality has been established beyond all question. We assert only that the demands

of the scientific method have been met within what we consider to be reasonable limits and that the time has come, for us at least, to accept the physical reality of the solar signal as what might be called the most appropriate, if not the only appropriate, working hypothesis of the moment. As before, we invite our readers to share this view." (Hines and Halevy, 1977).

An example of the amount of organization that existed during the winters 1963-1973 is shown in Figure 2 (Wilcox, 1979). The northern hemisphere was divided into seven zones with approximately the same area in each zone. Within each zone an analysis similar to that shown in Figure 1 was computed except that the VAI was computed as the area within vorticity contours of a single value, which was in successive analyses 20, 22, 24...30  $\times 10^{-5} \text{ s}^{-1}$ . The fractional effect shown as the ordinate in Figure 2 is simply the depth of the minimum in Figure 1 divided by the average value during adjacent days. The zones are largely independent since an individual region of high vorticity would usually be in one or at most two zones. The minimum was found in each of these zones, and within each zone the areas with more intense circulation (represented by larger values of vorticity) had a deeper minimum after the sector boundary transit. This amount of organization appears unlikely to be associated with a statistical excursion.

## 2. Temporal Changes in VAI Computed from NMC Data

Williams and Gerety (1978) claimed that the minimum discussed above diminished or disappeared during the winters 1974-1976 that followed the original analysis. In response we cited a discovery by Hines and Halevy (1977). They defined for each boundary an "Excursion" as being the range in VAI (maximum value minus minimum value) during a 12 day window centered on the time of the boundary. As shown in Figure 3 (Wilcox and Scherrer, 1981), boundary crossings that occurred during times of larger Excursions were followed by a minimum whose depth did not change with time from 1965 through 1977. Boundary crossings that occurred during times of smaller Excursions showed a null effect during most of the years shown in Figure 3.

Why then did Williams and Gerety (1978) report that the effect had diminished? The explanation is found in Figure 4 (Wilcox and Scherrer, 1981), which shows for each winter between 1963 and 1978 the number of boundary crossings that occurred during times of larger Excursions and during of times of smaller Excursions. During the interval 1963-1973 that was discussed by Wilcox et al. (1976) the number of boundaries with larger Excursions was approximately equal to the number of boundaries with smaller Excursions. After 1974 this situation changed dramatically, and in 1977 there were no boundaries with larger Excursion and in 1978 only one such boundary.

Now that a few more years have gone by it is possible to get a broader perspective on the change with time of the VAI as computed from the National Meteorological Center 500 mb height grid. Figure 5 shows a plot of VAI from 1964 through 1981. In the first years the average value of the VAI is larger, and a very clear seasonal variation is evident, both in the maximum values of the index and in the minimum values of the index. In the latter half of Figure 5 a steady decrease in average value of the VAI is evident, and the seasonal variation that was so clear in the early years is much less evident. In fact during the last years shown in Figure 5 the seasonal variation in the minimum of the VAI is almost absent. Our discussions with the National Meteorological Center have revealed that in recent years the 500 mb height grid has been subjected to increasing amounts of spatial smoothing in order to remove noise. "There is ample reason to believe that, the data set (500 mb height and winds) may well be inhomogeneous for the VAI computation" (Gerrity, 1982).

We believe that this increased smoothing during the data processing has removed completely the intervals of large excursion that were shown in Figure 3 to be associated with the effect. It is therefore not possible to make any statement about whether or not the effect reported by Wilcox et al. (1973) continued in the years after the original analysis.

Figure 6a shows an analysis similar to Figure 1 for the winters 1963-1973, and Figure 6b shows the same analysis for the

winters 1979-1982. Figure 6b shows a null effect in these years, but the average value of the VAI is only  $30 \times 10^5 \text{ km}^2$  as compared with an average value of  $50 \times 10^5 \text{ km}^2$  in Figure 6a. It is exceedingly unlikely that the average area of high-vorticity regions is now only 3/5 as large as it was ten years ago.

Since it is also possible to compute the VAI directly from winds, we obtained the National Meteorological Center 500 mb winds grids in digital form as archived by the National Center for Atmospheric Research in the hope that perhaps less smoothing had been applied to this data set. Figure 7 shows the VAI computed from winds as a function of time from 1965 through 1981. We see that the average VAI in 1972 was about half the average in 1971 and before, and that the years after 1972 average less than half as much as the years before 1972. Again the seasonal variation in both maxima and minima is very apparent before 1972 and much less prominent after. This winds grid data set is thus also inhomogeneous for VAI computations.

### 3. Noise in the VAI Computed from LFM Data

Larsen and Kelley (1977) supported the result shown in Figure 1 in an analysis using the Limited Area Fine Mesh (LFM) Grid that includes most of the North American continent. They further reported that on the two days following a sector boundary crossing the accuracy of forecasts of the VAI was considerably less than average. Larsen and Kelley analyzed the winters 1972 to 1975.

In the hope of extending this interesting investigation into later years we made use of the LFM grid as archived in digital form by the National Center for Atmospheric Research. We discovered that a change in the method of processing the LFM data on December 2, 1974 introduced noise into all subsequent computations of the VAI to such an extent that it is impossible to extend the investigations of Larsen and Kelly. The nature of this noise is illustrated in the following figures: Figure 8a shows 500 mb height contours for December 1, 1974, the last day that was free of the noise. Figure 8b shows the corresponding vorticity contours. Figure 9a shows 500 mb height contours for December 3, 1974. Note the small zig-zags in the encircled height contour. These lead to the diamond-like noise contours when vorticity is computed, as shown in Figure 9b. Each LFM grid from December 3 to the present time shows similar noise characteristics. Figure 10 is the average vorticity computed for the month of November 1975. The largest amplitude noise is in the approximate geographical locations of the Rocky Mountains and the Sierra Nevada Mountains.

We have been informed by the National Meteorological Center that the onset of this noise on and after December 3, 1974 can be identified with a change in their processing procedure on that date.

4. ACKNOWLEDGEMENTS

We thank Roy Jenne, Joseph P. Gerrity Jr. and J. Paul Dalla-valle for assistance with this work. This work was supported in part by the Office of Naval Research under Contract N00014-76-C-0207, by the National Aeronautics and Space Administration under Grant NGR05-020-559 and Contract NAS5-24420, by the Atmospheric Sciences Section of the National Science Foundation under Grant ATM77-20580 and by the Max C. Fleischmann Foundation.

5. REFERENCES

Gerrity, J.P. Jr., Chief Atmospheric Modeling Branch, National Meteorological Center: 1982, Private Communications.

Hines, C.O. and Halevy, I.: 1975, Nature, 258, 313.

Hines, C.O. and Halevy, I.: 1977, J. Atmos. Sci., 34, 382.

Larsen, M.F. and Kelley, M.C.: 1977, J. Geophys. Res. Lett., 4, 337.

Roberts, W.O. and Olson, R.H.: 1973, Rev. Geophys. Space Phys., 11, 731.

Wilcox, J.M. et al.: 1973, Science, 180, 185.

Wilcox, J.M., et al.: 1974, J. Atmos. Sci., 31, 581.

Wilcox, J.M., et al.: 1976, J. Atmos. Sci., 33, 1113.

Wilcox, J.M.: 1979, Solar-Terrestrial Influences on Weather & Climate, 149.

Wilcox, J.M. and Scherrer, P.H.: 1981, Solar Phys., 74, 421.

Williams, R.G. and Gerety, E.J.: 1978, Nature, 275, 200.

## FIGURE CAPTIONS

**Figure 1.** Superposed epoch analysis of the 500 mb vorticity area index (the area of low pressure troughs in the Northern Hemisphere) about times when solar magnetic sector boundaries were carried past the earth by the solar wind. The VAI is influenced by the large-scale solar sector structure, not by the boundary passages as such. Figure 1a uses 50 of the 54 boundaries used in the original work, Figure 1b uses 81 new boundary passages not included in the original analysis, and Figure 1c is a subset of Figure 1b in which the time of 46 boundary passages were determined from spacecraft observations (Wilcox et al, 1976).

**Figure 2.** The fractional depth of the sector-related minimum in vorticity area index as a function of the vorticity value used in computing the index (Wilcox, 1979).

**Figure 3.** The size of the Sun-Weather effect for the groups of boundary transits having larger Excursions (open circles) and for the groups of boundary transits having smaller Excursions (filled circles). The total length of the error bar is twice the standard error of the mean (Wilcox and Scherrer, 1981).

**Figure 4.** The number of boundary transits in each year for which the Excursions are in the larger group (open circles)

and in the smaller group (filled circles). Note that the intensity of tropospheric circulation as measured by the VAI declined after 1974 and decreased very much after 1976 (Wilcox and Scherrer, 1981).

**Figure 5.** The VAI computed from the National Meteorological Center height grid at 500 mb as a function of time from 1964 through 1981.

**Figure 6a.** Similar to Figure 1, showing a superposed epoch analysis of the 500 mb VAI about sector boundary transits in the winters 1964-1973. Note that the average value of the VAI is about  $50 \times 10^5 \text{ km}^2$ .

**Figure 6b.** The same as Figure 6a, except for the winters 1979-1982. The minimum in VAI after sector boundary transit that was so persistent in the original analysis is not present, but note that the average value of the VAI is now only about  $30 \times 10^5 \text{ km}^2$ .

**Figure 7.** The VAI computed from the National Meteorological Center winds grid at 500 mb from 1965 through 1981.

**Figure 8a.** Height contours at 500 mb in the Limited Area Fine Mesh Grid of the National Meteorological Center for December 1, 1974 at 0 z.

**Figure 8b.** Contours of vorticity calculated from Figure 8a.

**Figure 9a.** The same as Figure 8a, but for December 3, 1974 0 z.

Note the zig-zags in the encircled contour.

**Figure 9b.** Contours of vorticity calculated from Figure 9a.

Note the diamond-shaped noise contours that are most prominent on the left hand half of the figure.

**Figure 10.** The same as Figure 9b, but averaged over the month of November 1975 to bring out the noise contours more clearly.

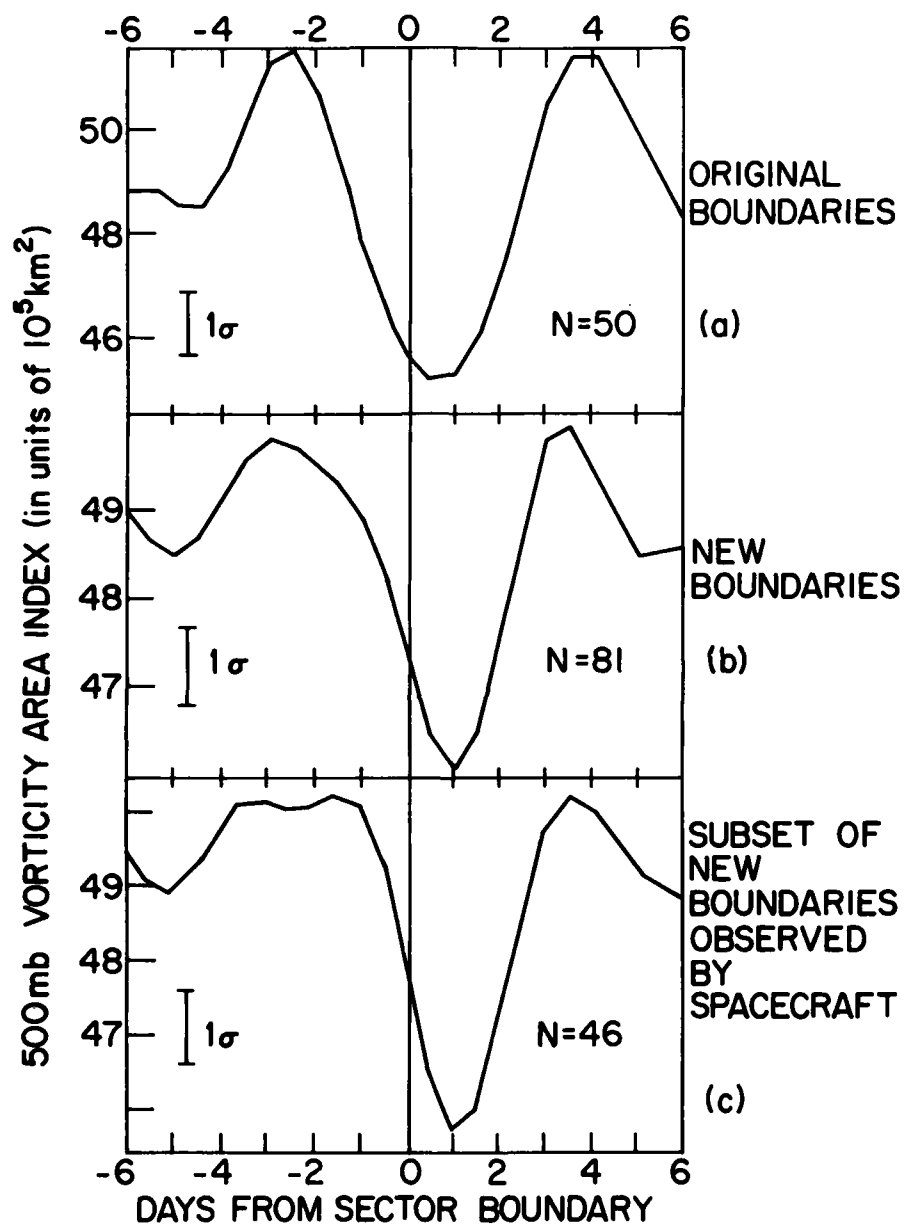


Fig. 1

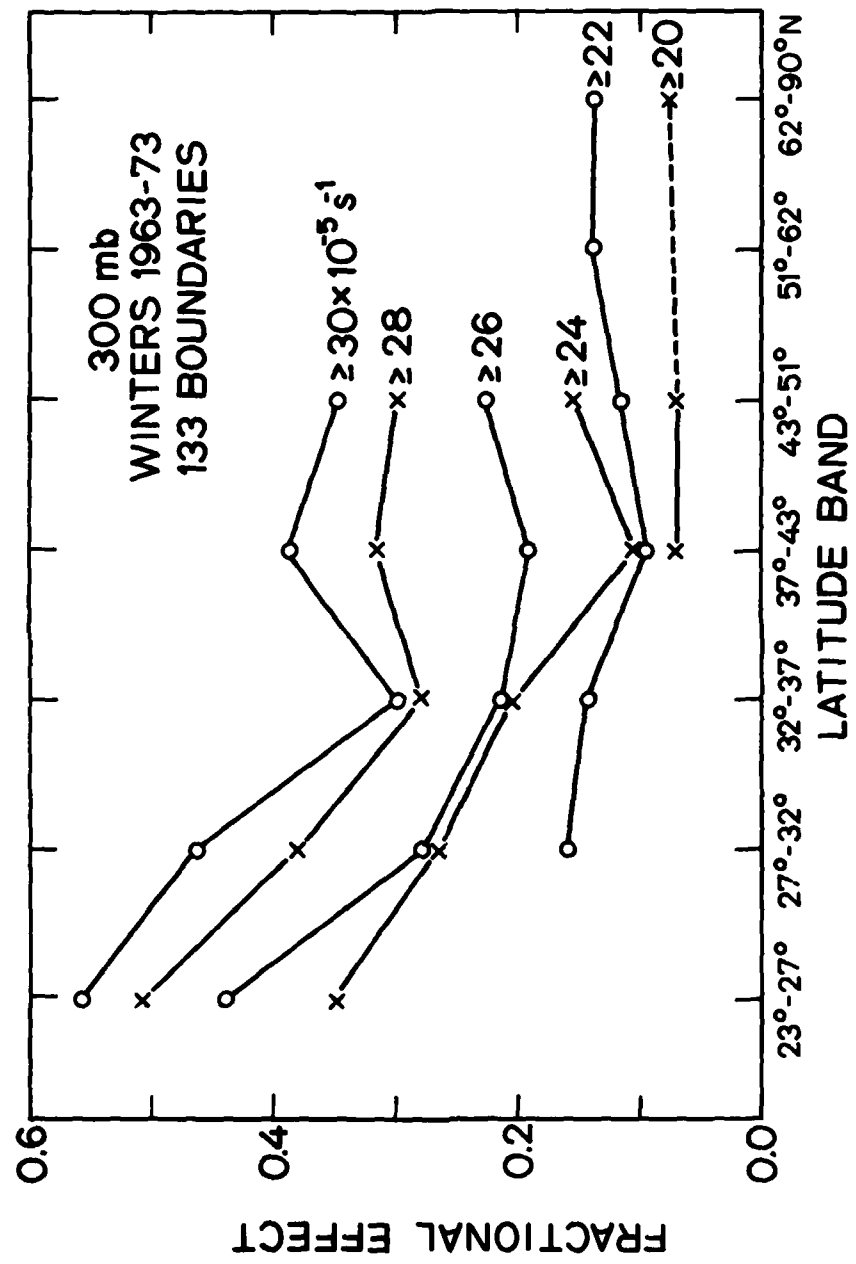


Fig. 2

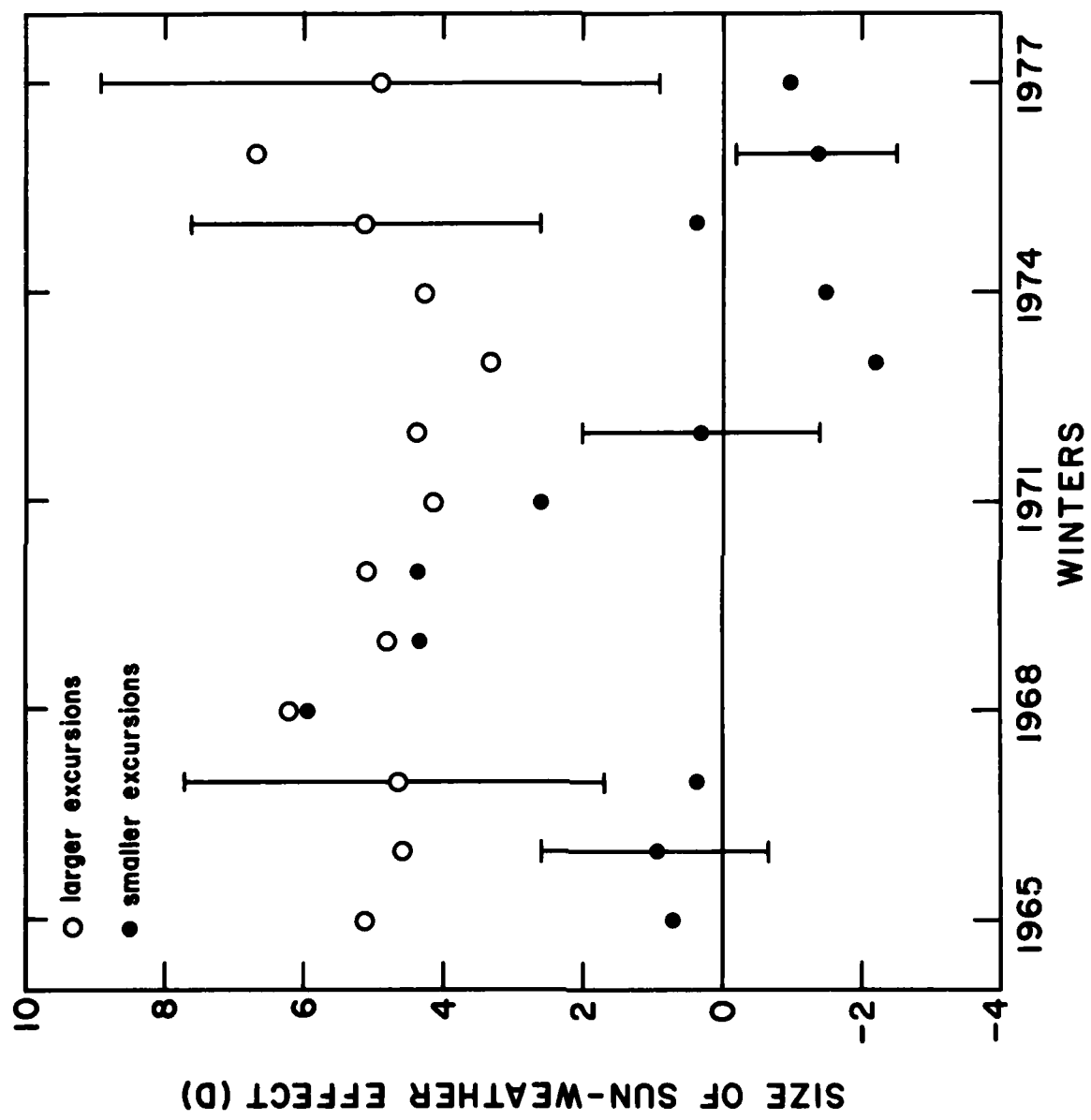


Fig. 3

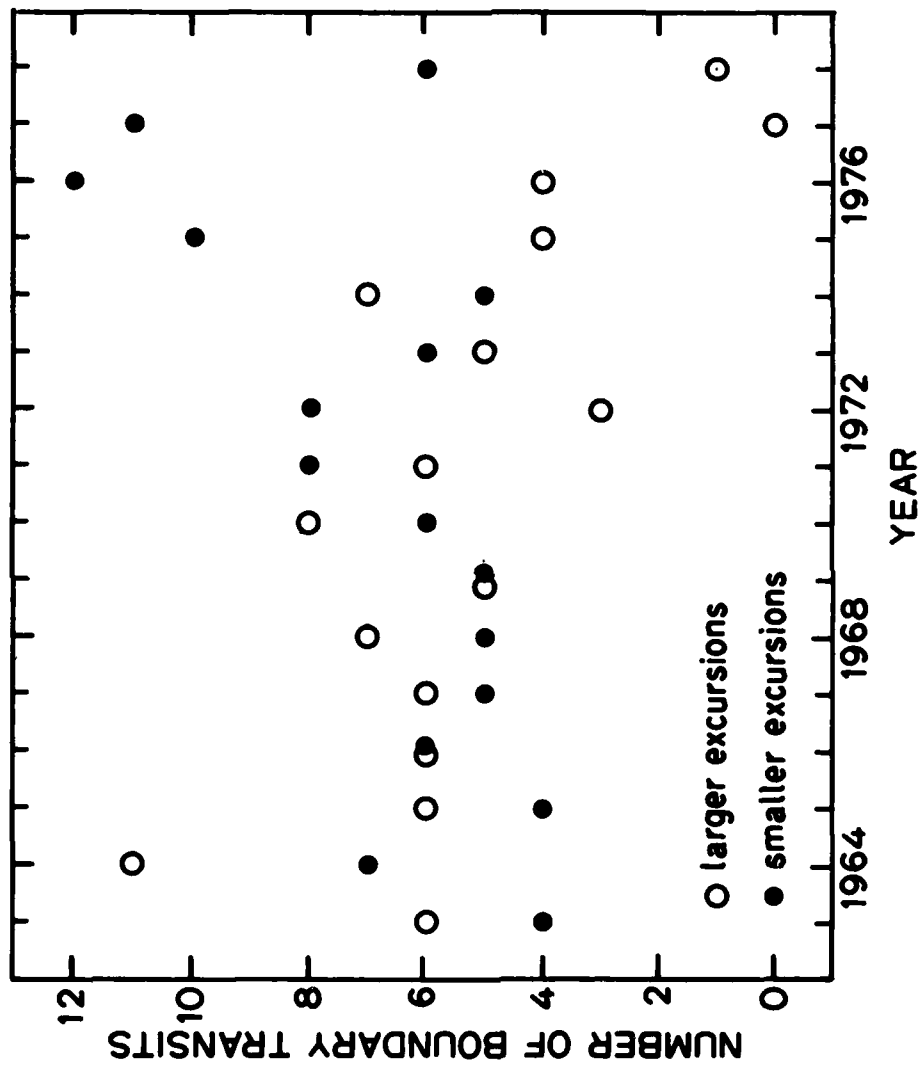


Fig. 4

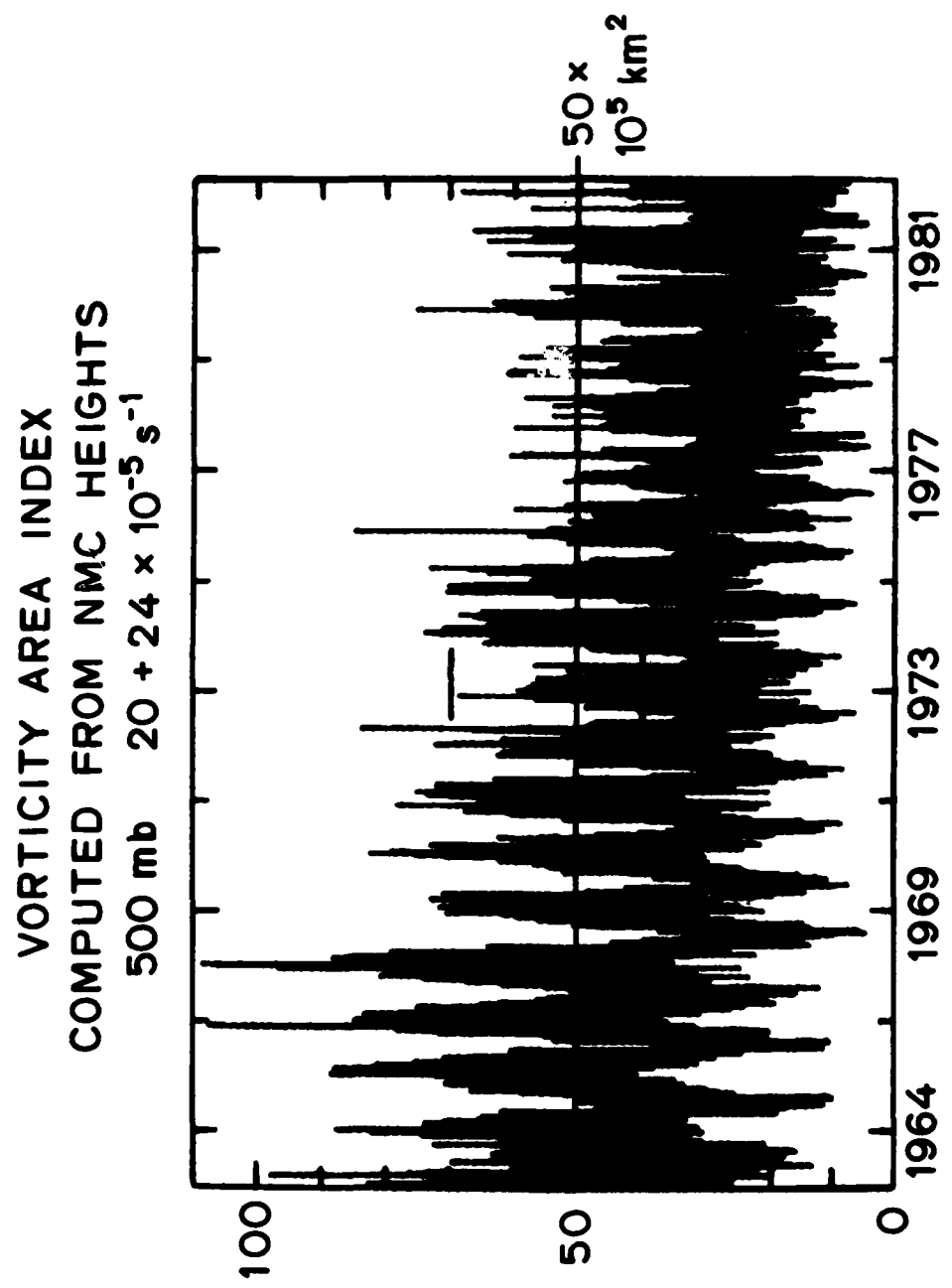


Fig. 5

VORTICITY AREA INDEX  
COMPUTED FROM NMC HEIGHTS  
500 mb  $20 + 24 \times 10^{-5} \text{ s}^{-1}$   
WINTERS 1964 - 1973

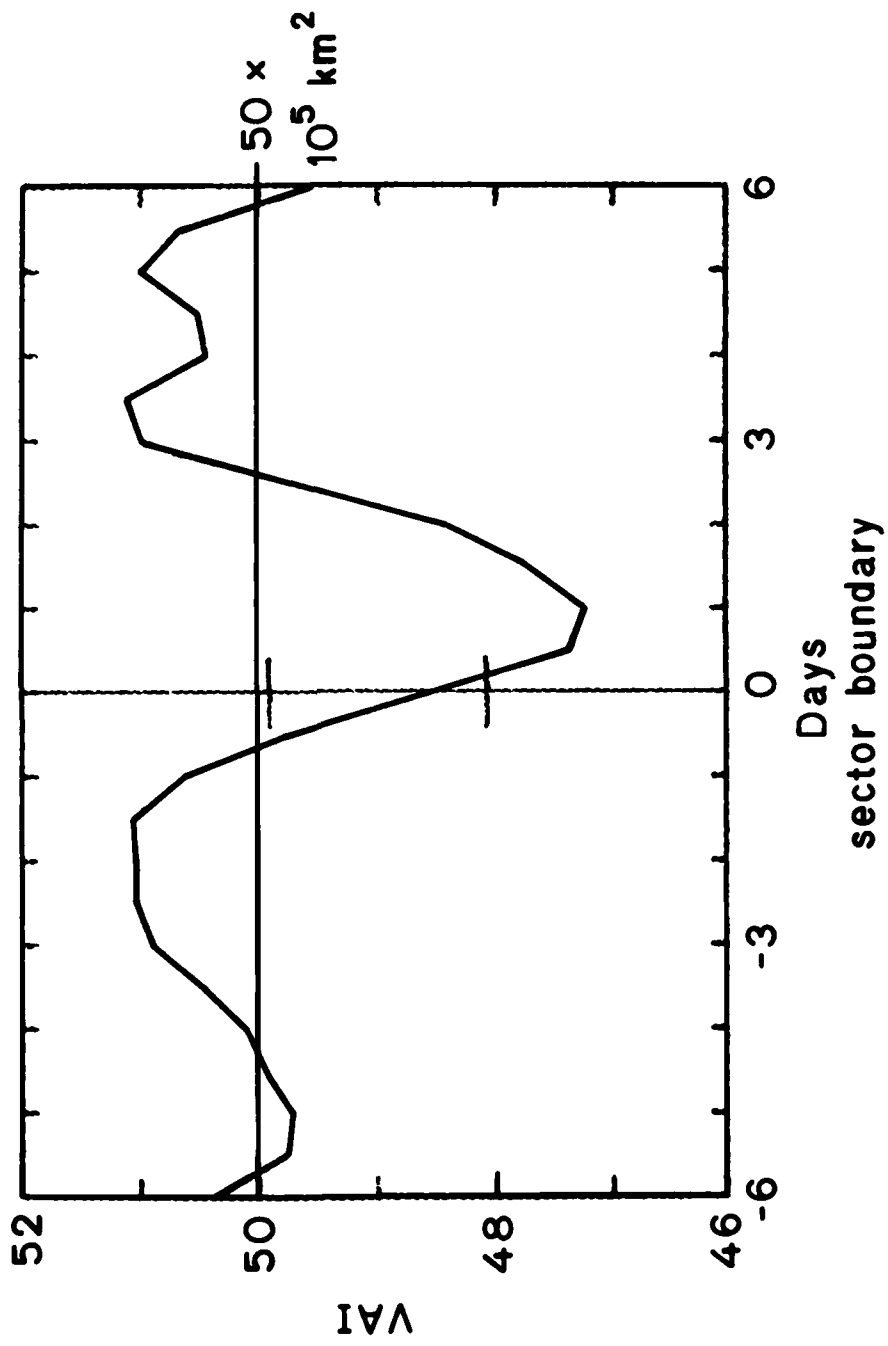


Fig. 6a.

VORTICITY AREA INDEX  
COMPUTED FROM NMC HEIGHTS  
500 mb  $20 + 24 \times 10^{-5} \text{ s}^{-1}$   
WINTERS 1979 - 1982

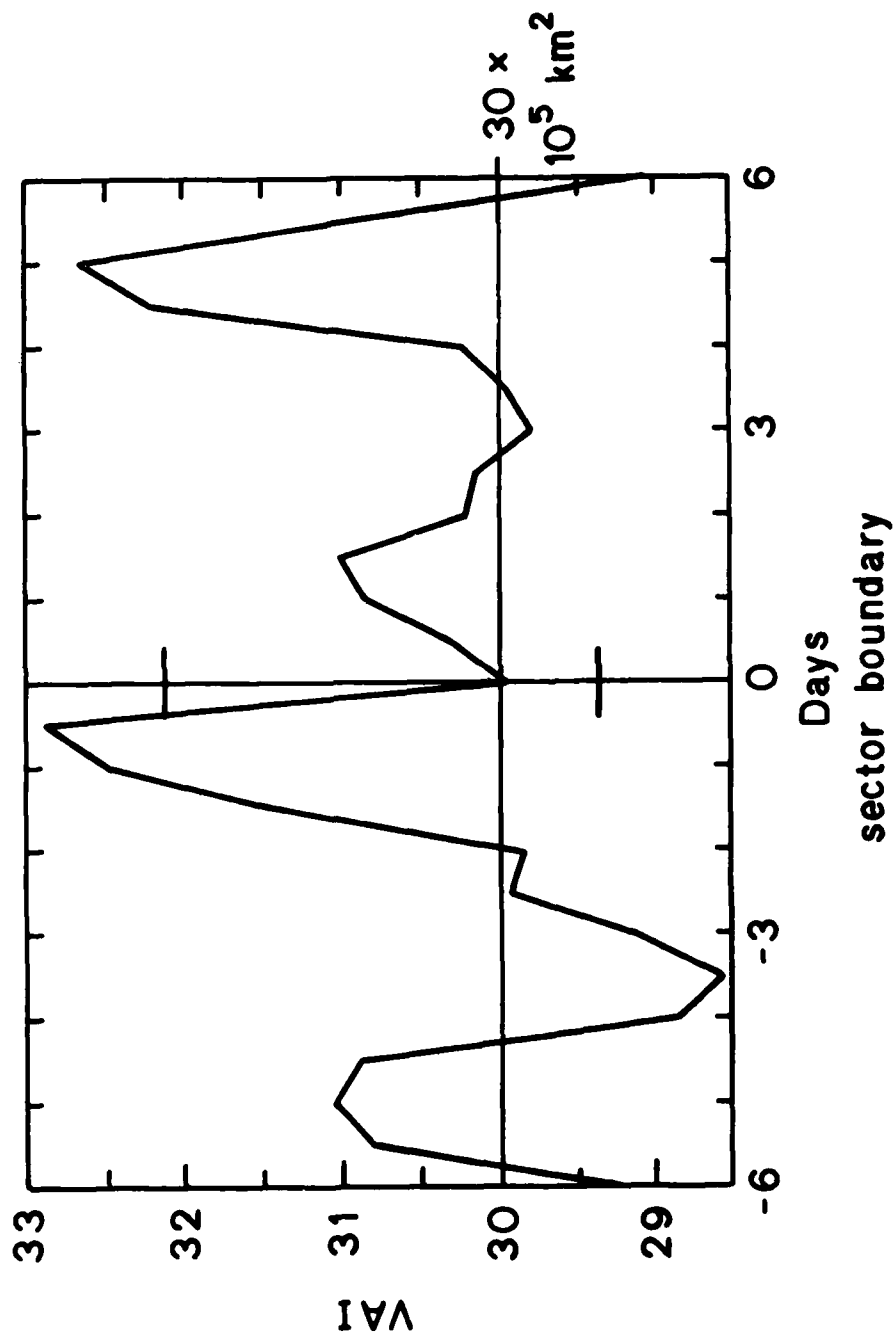


Fig. 6b.

VORTICITY AREA INDEX  
COMPUTED FROM NMC WINDS  
500 mb  $20 + 24 \times 10^{-5} \text{ s}^{-1}$

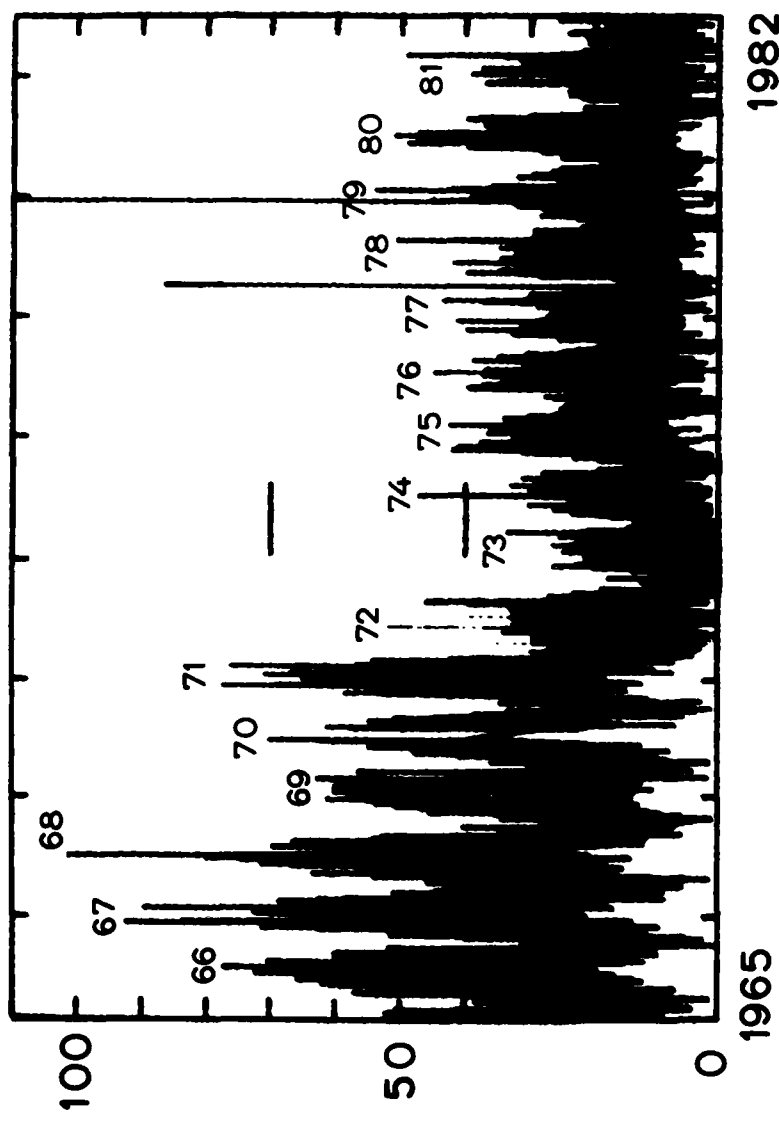


Fig. 7

LIMITED AREA FINE MESH GRID  
500 mb HEIGHT CONTOURS  
DECEMBER 1, 1974 0<sup>h</sup>

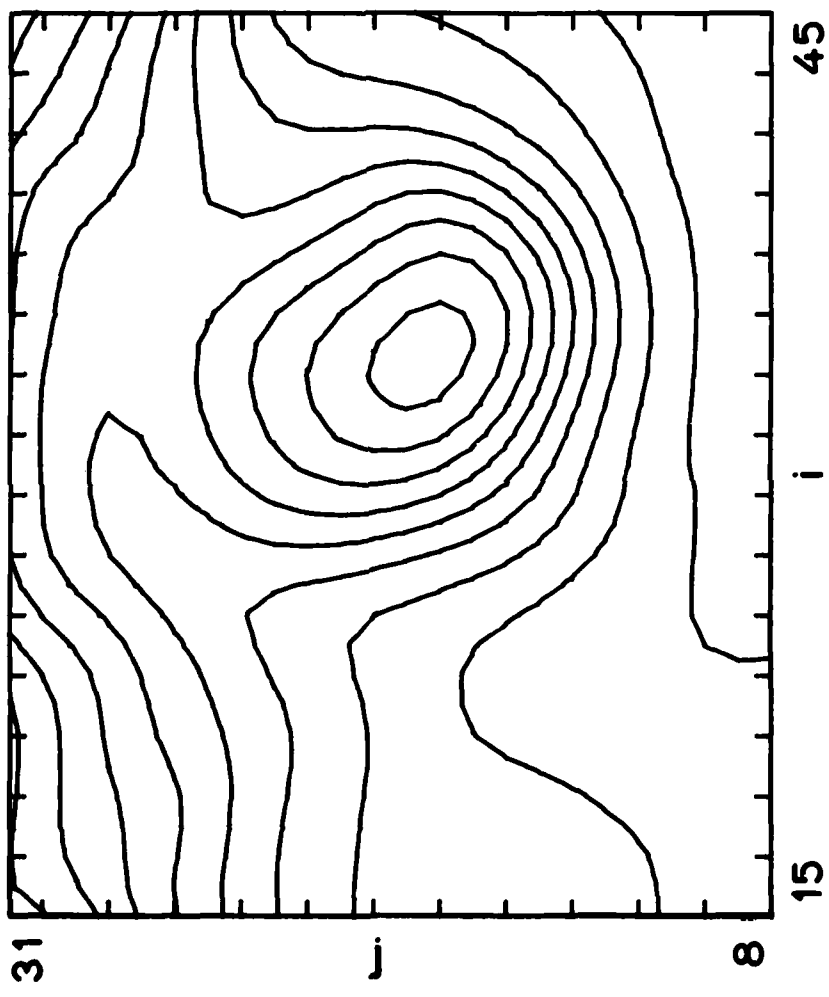


Fig. 8a

LIMITED AREA FINE MESH GRID  
500 mb VORTICITY CONTOURS  
DECEMBER 1, 1974 0<sup>h</sup>

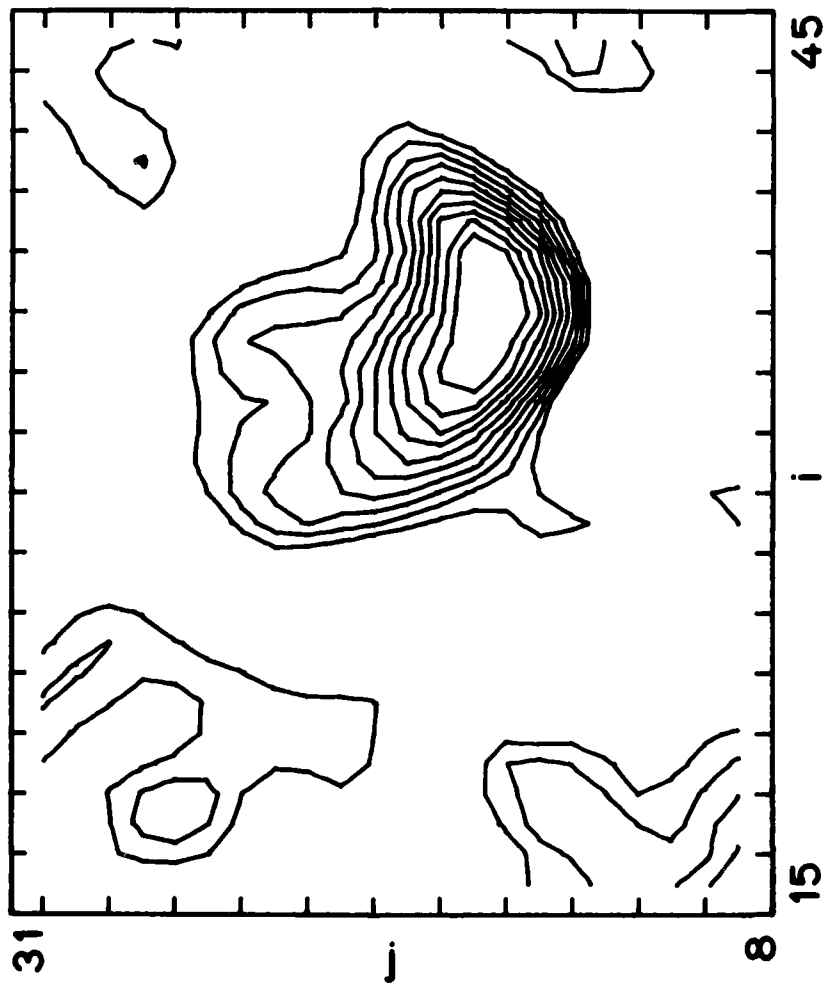


Fig. 8b

LIMITED AREA FINE MESH GRID  
500 mb HEIGHT CONTOURS  
DECEMBER 3, 1974 0<sup>h</sup>

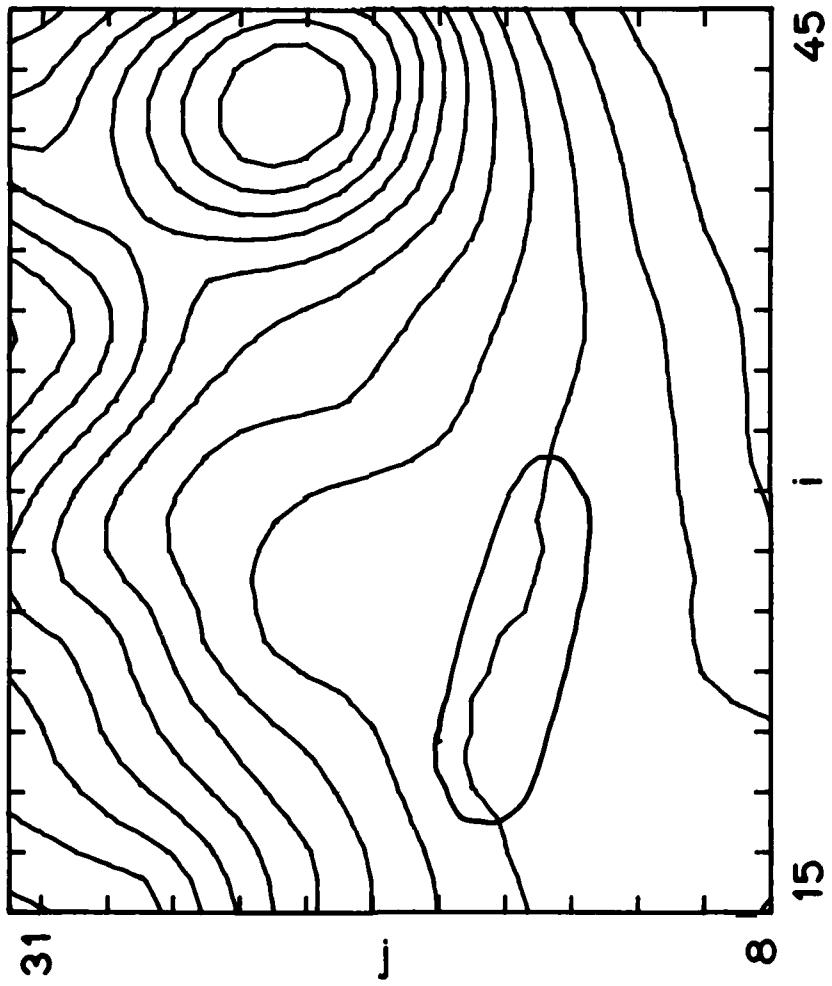


Fig. 9a.

LIMITED AREA FINE MESH GRID  
500 mb VORTICITY CONTOURS  
DECEMBER 3, 1974 0<sup>h</sup>

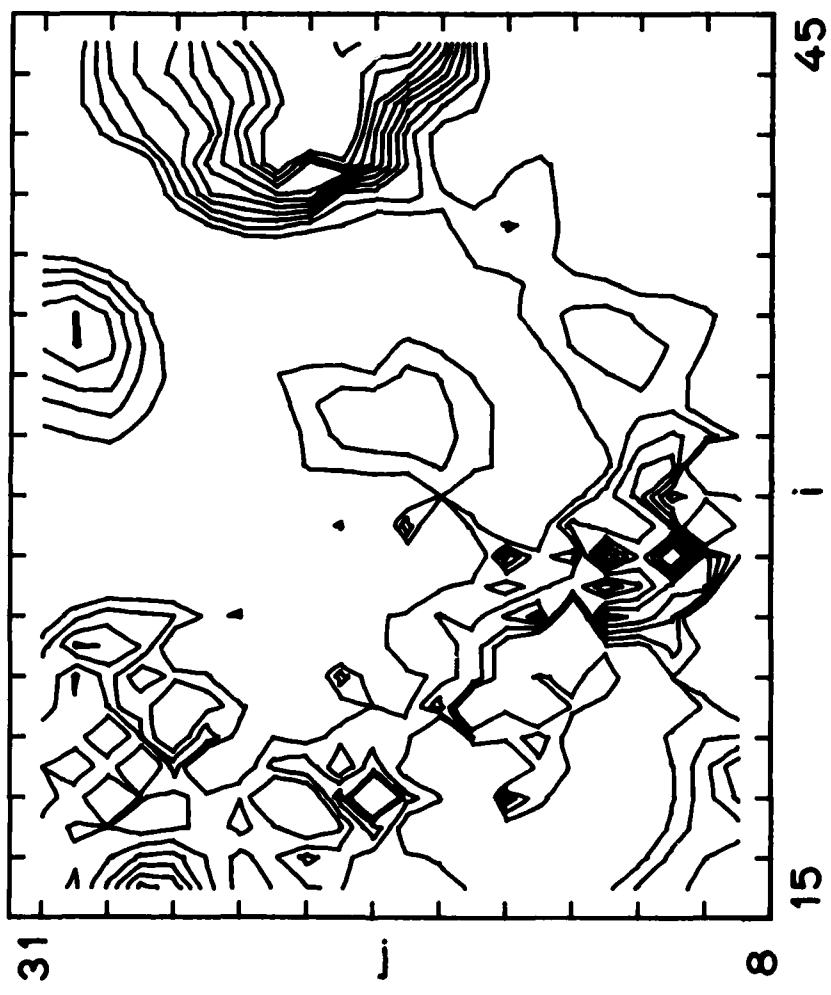


Fig. 9b.

LIMITED AREA FINE MESH GRID  
500 mb VORTICITY CONTOURS  
AVERAGE OF NOVEMBER 1975

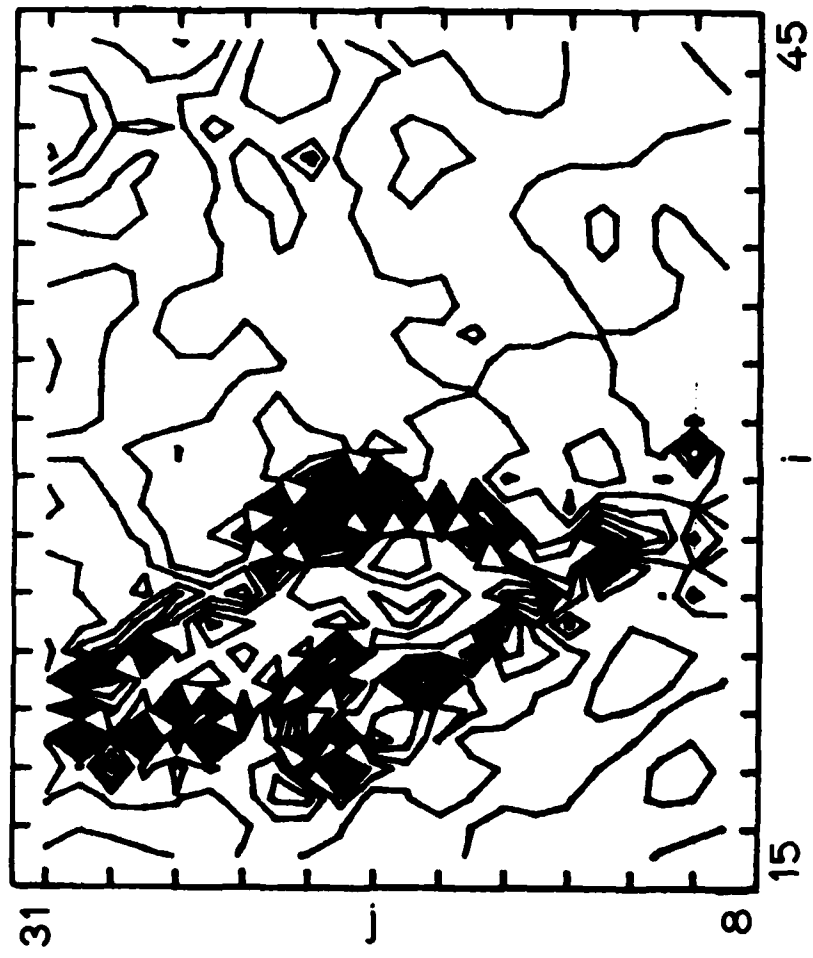


Fig. 10

## UNSTEADY, THERMALLY CONDUCTIVE CORONAL FLOW

STEVEN T. SUESS

Institute for Plasma Research, Stanford University, and Space Environment Laboratory,  
National Oceanic and Atmospheric Administration  
Received 1981 November 6; accepted 1982 February 23

### ABSTRACT

A numerical algorithm using implicit time-differencing is applied to the solar wind equations allowing, for the first time, solutions including thermal conduction to be found for time-dependent flow traversing the subsonic to supersonic velocity transition region. Sample solutions are shown that demonstrate the distinctive differences introduced by including thermal conduction, in comparison to the commonly available solutions assuming polytropic flow. Also, it is found that steady solutions are produced at least as quickly using a time-dependent relaxation to the steady state as when solving the steady-state equations.

*Subject headings:* hydromagnetics — Sun: corona — Sun: solar wind

### I. INTRODUCTION

Numerical solutions of the time-dependent solar wind equations have been appearing for several years, usually in the context of modeling a transient effect in the solar atmosphere or interplanetary medium. In order to avoid problems associated with treatment of boundary conditions near the Sun, in a subsonic flow regime, most of these solutions have been confined to regions where the flow is strictly supersonic (see, e.g., Hundhausen and Gentry 1969; Steinolfson, Dryer, and Nakagawa 1975; Metzler *et al.* 1979; Pizzo 1980). These solutions have nevertheless dealt with several important physical processes in the interplanetary medium, such as magnetic field effects (Steinolfson, Dryer, and Nakagawa 1975) and multiple species interactions with thermal conduction (Metzler *et al.* 1979). In contrast, other solutions have specifically addressed transient processes in the corona, dealing with the boundary condition problem in two different ways. One approach has been to take an initially hydrostatic atmosphere with nonreflective boundary conditions at the outer boundary (see, e.g., Han, Wu, and Nakagawa 1981 for a very comprehensive model using this approach). In a second approach, the boundary conditions at the base in the presence of an expanding corona have been treated in a self-consistent manner (Nakagawa and Steinolfson 1976; Steinolfson and Nakagawa 1976). This normally leads to more mathematical complexity, but has been found to be necessary in view of the fact that the corona cannot be approximated as hydrostatic above a fraction of a solar radius beyond the photosphere.

An important limitation in the analyses of Nakagawa and Steinolfson (1976) and Steinolfson and Nakagawa (1976) is their assumption of adiabatic flow. Here, an analysis is described which is specifically designed to overcome this limitation and to improve the efficiency with which both steady and transient solutions to the solar wind equations can be found. Specifically, an implicit (see, e.g., Richtmyer and Morton 1967 for a definition of the terms *explicit* and *implicit*) finite difference scheme is developed for the numerical solution of the solar wind equations including thermal conduction, for cases where the flow is subsonic near the Sun and supersonic far from the Sun. It is the intent in this paper to describe the analysis and numerical algorithm in some detail and to present results comparing transient effects in the corona for polytropic flow with those for thermally conductive flow.

To the best of this author's knowledge, implicit differencing schemes have been applied to the solar wind equations in only two published instances. In the first case Metzler *et al.* (1979) used this approach to solve the time-dependent two-fluid equations in the supersonic flow regime. In the second, Han, Wu, and Nakagawa (1981) analyzed coronal transients on a hydrostatic initial state, in two dimensions, with a magnetic field. Metzler *et al.* used implicit differencing in order to be able to include thermal diffusion, whereas Han *et al.*, although initially including thermal diffusion, only showed results for a transient in a polytropic gas. The reason Han *et al.* turned to implicit time differencing was that the limitation on step size due to the Courant condition (Richtmyer and Morton 1967) that applies to all explicit schemes was causing an impossibly small time step to be used for only moderately large magnetic field strengths.

In general, the solar wind equations are prime candidates for solution with implicit time-differencing because they are extremely "stiff"—that is, the propagation speed of a thermal pulse is much larger than the sound or Alfvén speeds. This can be demonstrated by comparing the characteristic time scales for propagation of a sound wave ( $\tau_s$ ) and

a thermal wave ( $\tau_c$ ). These are (Craig and McClymont 1976):

$$\tau_s \approx 8.3 \times 10^{-5} L/T^{1/2}, \quad \tau_c \approx 3 \times 10^{-10} n L^2/T^{5/2},$$

where  $L$ ,  $n$ , and  $T$  are the length scale (cm), electron number density ( $\text{cm}^{-3}$ ), and temperature. In the corona,  $L \sim 10^{11}$  cm,  $T \sim 10^6$  K, and  $n \sim 10^5 \text{ cm}^{-3}$ . For these numbers, the ratio ( $\tau_s/\tau_c$ ) is about 25, a large number for these purposes. This is the reason for the relative importance of thermal conduction in the present analysis in comparison to analyses describing transient motion near the transition region (Craig and McClymont 1976; Wu *et al.* 1981) where the density is much larger. Implicit schemes are not subject to the Courant numerical stability condition set by the largest characteristic speed, and so are stable for arbitrarily large time steps. The penalty for this stability is that implicit schemes are algebraically complex and hence have a large arithmetic operation count.

The above-mentioned applications of implicit time-differencing to the solar wind equations used classical algorithms developed early in the history of implicit schemes, and suffer as a consequence. Han, Wu, and Nakagawa (1981) utilize the implicit continuous-fluid Eulerian (ICE) method (see, e.g., Harlow 1973). The ICE method, although successfully applied to a large class of problems, is relatively cumbersome due to its use of a nonsimultaneous solution of the equations on a split grid. Metzler *et al.* (1980) solve the equations in a Lagrangian frame of reference, treating the energy equation implicitly but the momentum equations explicitly. Additional complexity results from an iterative technique utilized to account for the nonlinearity introduced by the transport coefficients. Recently, implicit methods have gained new stature from the development of concise, noniterative, one-dimensional and alternating direction implicit (ADI) multidimensional schemes by Lindemuth and Kileen (1973), Briley and McDonald (1975), and Beam and Warming (1978), among others. The paper by Beam and Warming (1978) will be used extensively in the discussion that follows, and so will simply be referred to as BW.

The BW algorithm, as applied here, is noniterative and retains as nearly a conservation law form as is possible for the solar wind equations. This is essential, together with the inclusion of dissipation, for the proper treatment of embedded shock waves ("shock capturing"). The temporal difference approximation is generalized to retain a variety of schemes including a three-level scheme requiring only two levels of data storage. The development makes extensive use of the BW "delta" form (increments of the conserved variable and flux vectors) to achieve numerical efficiency and retain the property of a steady state (if one exists) independent of the time step.

In the following section, the physics of the model and the equations of motion are stated and discussed. The implicit algorithm is developed in § III, and a description is given of how artificial dissipation should be added to the algorithm in those cases for which it is found necessary (e.g., shock propagation) in § IV. Section V contains a discussion of the boundary condition treatment for steady and time-dependent flows, and examples are described in § VI. Additions to the equations and modifications of the algorithm to address important questions in solar and stellar wind studies are discussed in § VII, and the results are summarized in § VIII.

## II. MODEL DESCRIPTION

The model equations are for a radial (spherically symmetric) flow, one-fluid description of the proton-electron solar wind with no momentum or energy addition, and no "superradial divergence." This set of equations is sufficiently comprehensive to produce interesting new results in modeling transient processes. The mass, momentum, and energy conservation equations for this ensemble of assumptions and model descriptions are then usually written:

$$\frac{\partial \rho}{\partial t} + \frac{1}{r^2} \frac{\partial}{\partial r} (r^2 \rho v_r) = 0, \quad (1)$$

$$\rho \left( \frac{\partial v_r}{\partial t} + v_r \frac{\partial v_r}{\partial r} \right) = - \frac{\partial p}{\partial r} - \rho \frac{GM}{r^2}, \quad (2)$$

$$\frac{\partial e}{\partial t} + \frac{1}{r^2} \frac{\partial}{\partial r} [r^2 v_r (e + p)] + \frac{1}{r^2} \frac{\partial}{\partial r} (r^2 q) + \rho v_r \frac{GM}{r^2} = 0, \quad (3)$$

where  $\rho$  is the density,  $v_r$  is the radial velocity,  $p$  is the pressure,  $T$  is the temperature,  $q$  is the heat flux density,  $e$  is the total (kinetic plus internal) energy per unit volume, and  $M$  is the mass of the Sun. The density is related to the number density of protons and electrons by

$$\rho = n(m_p + m_e); \quad (4)$$

and the perfect gas law is used:

$$p = 2nkT = 2\rho \left( \frac{k}{m_p + m_e} \right) T \equiv 2\rho RT,$$

$$R \approx 8.317 \times 10^7 \text{ (cgs).} \quad (5)$$

As the intent here is to compare polytropic flow with the consequences of the presence of strictly classical conduction, the form chosen for  $q$ , the heat flux density, is the collision dominated model described by Spitzer (1962):

$$q = -\kappa T^{5/2} \frac{\partial T}{\partial r}, \quad (6)$$

$$\kappa = \frac{1.99 \times 10^{-5}}{\ln \Lambda} \text{ (cgs),} \quad (7)$$

$$\Lambda \approx 1.246 \times 10^4 (T^3/n)^{1/2}. \quad (8)$$

Equations (6)–(8) differ from analogous choices in some other models (e.g., Holzer and Leer 1981; Whang and Chang 1965) in including the spatial variation of the logarithmic term in (8). This is usually a small effect, but it is easily included in the analysis and so shall be retained. Because this collisional model for  $q$  is valid only near the base of the corona, the computational examples in section 6 will not be carried beyond about 20 solar radii.

Putting equations (1)–(3) into near “conservation law” form gives:

$$\frac{\partial b}{\partial t} + \frac{\partial m_r}{\partial r} = 0, \quad (9)$$

$$\frac{\partial m_r}{\partial t} + \frac{\partial}{\partial r} \left( \frac{m_r^2}{b} + r^2 p \right) - 2rp - b \frac{GM}{r^2} = 0, \quad (10)$$

$$\frac{\partial \epsilon}{\partial t} + \frac{\partial}{\partial r} \left[ \frac{m_r}{b} (\epsilon + r^2 p) \right] - \frac{\partial}{\partial r} \left( r^2 \kappa \frac{\partial T}{\partial r} \right) + m_r \frac{GM}{r^2} = 0, \quad (11)$$

where

$$b = \rho r^2 \quad (12a)$$

$$m_r = \rho v_r r^2, \quad (12b)$$

$$\epsilon = er^2 \quad (12c)$$

are the conserved variables related to the mass, momentum, and energy densities, respectively. The equation of state is now

$$p = \frac{\gamma-1}{r^2} \left( \epsilon - \frac{1}{2} \frac{m_r^2}{b} \right), \quad (13)$$

where  $\gamma$  is the ratio of specific heats (or the polytropic index in case thermal conduction is not included). The temperature is given by

$$T = \frac{1}{2Rb^2} (\gamma-1) \left( \epsilon b - \frac{1}{2} m_r^2 \right) \quad (14)$$

Equations (9)–(11) can also be written in the vector form:

$$\frac{\partial \mathbf{U}}{\partial t} + \frac{\partial \mathbf{F}(\mathbf{U})}{\partial r} + \frac{\partial \mathbf{V}(\mathbf{U}, \mathbf{U}_r)}{\partial r} + \mathbf{H} = 0, \quad (15)$$

where the vectors  $\mathbf{U}$ ,  $\mathbf{F}$ ,  $\mathbf{V}$ , and  $\mathbf{H}$  can be deduced from (9)–(11) by inspection (see Appendix, [A1]–[A4]) and  $U_r = \partial \mathbf{U} / \partial r$ . This vector equation, together with boundary conditions to be discussed later, constitutes the complete description of the problem.

### III. ALGORITHM FOR SOLUTION BY IMPLICIT TIME-DIFFERENCING

In (15),  $\mathbf{U}$  is the vector of conserved variables,  $\mathbf{F}$  and  $\mathbf{V}$  are flux vectors, and  $\mathbf{H}$  is the inhomogeneous part of the equation. The treatment of this equation in this section, along with the development of the implicit algorithm, will closely follow the discussion in BW, to which the reader is referred for more details.

For advancing the solution in time, BW suggest a general single-step temporal scheme that can be written in the form:

$$\Delta \mathbf{U}^n = \frac{\lambda \Delta t}{1+\xi} \frac{\partial \Delta \mathbf{U}^n}{\partial t} + \frac{\Delta t}{1+\xi} \frac{\partial \mathbf{U}^n}{\partial t} + \frac{\xi}{1+\xi} \Delta \mathbf{U}^{n-1} + O[(\lambda - \frac{1}{2} - \xi) \Delta t^2 + \Delta t^3], \quad (16)$$

where

$$\mathbf{U}^n = \mathbf{U} \left( \sum_{l=1}^n \Delta t_l \right) \quad \text{and} \quad \Delta \mathbf{U}^n = \mathbf{U}^{n+1} - \mathbf{U}^n.$$

Here, except for the first time step,  $\lambda = 1$  and  $\xi = \frac{1}{2}$ , which produces a three-level second order accurate scheme. At the first time step, because only one level of information will be available,  $\lambda = \frac{1}{2}$  and  $\xi = 0$ .

If (15) is solved for  $\partial \mathbf{U} / \partial t$  and the resulting expression for the temporal derivative is inserted in (16), then it can be shown that

$$\begin{aligned} \Delta \mathbf{U}^n = & \frac{\lambda \Delta t}{1+\xi} \left[ -\frac{\partial \Delta \mathbf{F}^n}{\partial r} - \frac{\partial \Delta \mathbf{V}^n}{\partial r} - \Delta \mathbf{H}^n \right] + \frac{\Delta t}{1+\xi} \left[ -\frac{\partial \mathbf{F}^n}{\partial r} - \frac{\partial \mathbf{V}^n}{\partial r} - \mathbf{H}^n \right] \\ & + \frac{\xi}{1+\xi} \Delta \mathbf{U}^{n-1} + O[(\lambda - \frac{1}{2} - \xi) \Delta t^2 + \Delta t^3], \end{aligned} \quad (17)$$

where

$$\mathbf{F}^n = \mathbf{F} \left( \sum_{l=1}^n \Delta t_l \right), \quad \Delta \mathbf{F}^n = \mathbf{F}^{n+1} - \mathbf{F}^n,$$

with similar definitions for  $\Delta \mathbf{V}^n$  and  $\Delta \mathbf{H}^n$ . Henceforth, having served its purpose, the order symbol  $O[(\lambda - \frac{1}{2} - \xi) \Delta t^2 + \Delta t^3]$  will be dropped. A problem arises because the vector increments  $\Delta \mathbf{F}^n$ ,  $\Delta \mathbf{V}^n$  and  $\Delta \mathbf{H}^n$  are nonlinear functions of the conserved variables,  $\mathbf{U}$ . A linear equation with the same temporal accuracy as (17) can be obtained if a Taylor series expansion is used (Briley and McDonald 1973; Beam and Warming 1976), such that

$$\mathbf{F}^{n+1} = \mathbf{F}^n + \left( \frac{\partial \mathbf{F}}{\partial \mathbf{U}} \right)^n (\mathbf{U}^{n+1} - \mathbf{U}^n) + O[\Delta t^2] \quad (18)$$

or

$$\Delta \mathbf{F}^n = \mathbf{A}^n \Delta \mathbf{U}^n + O[\Delta t^2], \quad (19a)$$

where  $\mathbf{A}$  is, in tensor notation, the Jacobian matrix  $\partial \mathbf{F} / \partial \mathbf{U}$  (Appendix, eq. [A5]). Significantly, this technique is described as the “most robust strategy for linearization” by Dwyer (1981). The terms in  $\mathbf{V}$  and  $\mathbf{H}$  can be treated similarly to give

$$\Delta \mathbf{V}^n = (\mathbf{C} - \mathbf{P}_r) \Delta \mathbf{U}^n + \frac{\partial}{\partial r} (\mathbf{P} \Delta \mathbf{U})^n + O[\Delta t^2], \quad (19b)$$

$$\Delta \mathbf{H}^n = \mathbf{E} \Delta \mathbf{U}^n + O[\Delta t^2], \quad (19c)$$

where  $\mathbf{C}$  is (in tensor notation) the Jacobian matrix  $\partial \mathbf{V} / \partial \mathbf{U}$ ,  $\mathbf{E}$  is the Jacobian matrix  $\partial \mathbf{H} / \partial \mathbf{U}$ ,  $\mathbf{P}$  is the Jacobian matrix  $\partial \mathbf{V} / \partial \mathbf{U}_r$ ,  $\mathbf{P}_r = \partial \mathbf{P} / \partial r$ , and  $\mathbf{U}_r = \partial \mathbf{U} / \partial r$ . These matrices are shown in detail in the Appendix (eqs. [A6]–[A9]).

Introducing the approximations (19) into (17) gives

$$\left\{ \mathbf{I} + \frac{\lambda \Delta t}{1+\xi} \left[ \frac{\partial}{\partial r} (\mathbf{A} + \mathbf{C} - \mathbf{P}_r)^n - \frac{\partial^2}{\partial r^2} (\mathbf{P})^n + (\mathbf{E})^n \right] \right\} \Delta \mathbf{U}^n = - \frac{\Delta t}{1+\xi} \left\{ \frac{\partial}{\partial r} (\mathbf{F} + \mathbf{V})^n + (\mathbf{H})^n \right\} + \frac{\xi}{1+\xi} \Delta \mathbf{U}^{n-1}, \quad (20)$$

where here, and throughout the remainder of the paper, notation of the form

$$\left[ \frac{\partial}{\partial r} (\mathbf{A} + \mathbf{C} - \mathbf{P}_r) \right] \Delta \mathbf{U}^n$$

denotes

$$\frac{\partial}{\partial r} [(\mathbf{A} + \mathbf{C} - \mathbf{P}_r) \Delta \mathbf{U}^n], \text{ etc.}$$

In (20), the right hand side of the equation can be recognized as the steady-state portion of equations (1)–(3) plus a term depending on  $\Delta \mathbf{U}^{n-1}$ . These parts of (20) only depend on information from the present and previous time-steps, and so are called the “explicit” portion of the equation. Conversely, the left hand side of (20) is all multiplied by  $\Delta \mathbf{U}^n$ , thereby depending on information at the advance time-step, and is consequently called the “implicit” portion of the equation.

The spatial derivatives in (20) are to be approximated by appropriate finite-difference quotients. When this is done, the symbol  $\mathbf{U}^n(r)$  is replaced by  $\mathbf{U}_i^n$  where

$$r_i = \sum_{l=1}^{i-1} \Delta r_l + r_0$$

( $r_0$  is the base radius, or the radius of the Sun),  $\Delta r_i = r_{i+1} - r_i$ , and  $r_1 = r_0$ . In constructing these differences, it will be important to allow for variable grid size (a slowly varying time step is already permitted with the scheme invoked, while retaining second order accuracy). For the computations used here, the following three-point second-order accurate central-difference approximations are used:

$$\left( \frac{\partial f}{\partial r} \right)_i = \frac{1}{2} \left[ \frac{f_{i+1}}{\Delta r_i} + f_i \left( \frac{1}{\Delta r_{i-1}} - \frac{1}{\Delta r_i} \right) - \frac{f_{i-1}}{\Delta r_{i-1}} \right] + O[\Delta r_i^2], \quad (21a)$$

$$\left( \frac{\partial^2 f}{\partial r^2} \right)_i = \frac{1}{2} \left[ \frac{f_{i+1}}{\Delta r_i} \left( \frac{1}{\Delta r_i} + \frac{1}{\Delta r_{i-1}} \right) - f_i \left( \frac{1}{\Delta r_i} + \frac{1}{\Delta r_{i-1}} \right)^2 + \frac{f_{i-1}}{\Delta r_{i-1}} \left( \frac{1}{\Delta r_i} + \frac{1}{\Delta r_{i-1}} \right) \right] + O[\Delta r_i^2]. \quad (21b)$$

Equation (21b) results from combining backward first-derivative approximations at  $\Delta r_i$  and  $\Delta r_{i+1}$  with forward first-derivative approximations at  $\Delta r_{i-1}$  and  $\Delta r_i$  to find the second derivative. This gives a form in which

$$\left( \frac{1}{\Delta r_i} + \frac{1}{\Delta r_{i-1}} \right)$$

can be factored out. A more conventional derivation is to use the average of  $\Delta r_i$  and  $\Delta r_{i-1}$ , together with two-point centered first-derivative approximations over  $\Delta r_i$  and  $\Delta r_{i-1}$ , to find the second derivative on a variable grid (Schnack 1978). These two approximations are equivalent to within  $O(\Delta r_i^2)$  times the rate of change of  $\Delta r_i$  with radius. Both (21a) and (21b) are strictly second order accurate only for slowly varying grid spacing. At the boundaries, (21a) and (21b) will be impossible to use, so at those grid points the following one-sided three-point backward and forward (respectively) approximations are used:

$$\left( \frac{\partial f}{\partial r} \right)_i = \frac{-(2\Delta r_{i-1}\Delta r_{i-2} + \Delta r_{i-2}^2)f_i + (\Delta r_{i-1} + \Delta r_{i-2})^2 f_{i-1} - \Delta r_{i-1}^2 f_{i-2}}{[\Delta r_{i-1}\Delta r_{i-2}(\Delta r_{i-1} + \Delta r_{i-2})]} \quad (22a)$$

$$\left( \frac{\partial f}{\partial r} \right)_i = \frac{-(2\Delta r_i\Delta r_{i+1} + \Delta r_{i+1}^2)f_i + (\Delta r_i + \Delta r_{i+1})^2 f_{i+1} - \Delta r_i^2 f_{i+2}}{[\Delta r_i\Delta r_{i+1}(\Delta r_i + \Delta r_{i+1})]} \quad (22b)$$

where the backward (forward) differencing scheme is to be applied at the outer (inner) grid point. Second derivatives at the boundaries, required when including dissipation, will be discussed in § IV.

Use of (21) in (20) produces a block-tridiagonal system of equations of the form:

$$X_{i-1}'' \Delta U_{i-1}'' + Y_i'' \Delta U_i'' + Z_{i+1}'' \Delta U_{i+1}'' = T_i'', \quad (23)$$

where  $X_{i-1}''$ ,  $Y_i''$ , and  $Z_{i+1}''$ , are matrices of dimension  $3 \times 3$ , and the  $T_i''$  are vectors. This system of equations can be solved using standard algorithms such as that described by Isaacson and Keller (1966) or by Varga (1962). In this application, the BW formulation contains three levels of data ( $n+1$ ,  $n$ , and  $n-1$ ); but only two levels of data,  $U_i''$  and  $\Delta U_i''$ , need be stored for each spatial grid point. This decreases the amount of computer memory required for these matrices by one-third.

At the start of the calculation, it is assumed that a complete description of the solar wind flow is provided at each grid point. This provides the initial state, but at only one time level. Consequently, as described earlier,  $\lambda = \frac{1}{2}$  and  $\xi = 0.0$  for the first time step. Thereafter, they are taken to be 1.0 and 0.5, respectively. The initial state is essentially arbitrary—it need not be a solution to the steady solar wind equations, although it will be such when modeling the transients described in § VI. Various choices will be discussed in § IV.

#### IV. ADDING DISSIPATION

The implicit generalized time-differencing scheme (16) is, as applied here, temporally dissipative except for the longest and shortest wavelengths (BW, § V). Since the phase error of the short wavelengths is large, it is sometimes necessary to add dissipative terms to the explicit portion of the equations to damp the short wavelengths. Apparently this introduces a new stability bound (Steger 1978), so Steger (private communication) suggests that a dissipative term also be added to the implicit portion of the equations. The terms chosen here, which are of the same form as those used by Steger (1978) and Steger and Bailey (1980), are shown below in the modified form of equation (20) to be used henceforth for the analysis:

$$\begin{aligned} & \left\{ \mathbf{I} + \frac{\lambda \Delta t}{1+\xi} \left[ \frac{\partial}{\partial r} (\mathbf{A} + \mathbf{C} - \mathbf{P}_r)'' + \frac{\partial^2}{\partial r^2} (\mathbf{P})'' + (\mathbf{E})'' - \epsilon_i \Delta r_i^2 \frac{u_c}{r_c} (\nabla \Delta)_i \right] \right\} \Delta \mathbf{U}'' \\ &= - \frac{\Delta t}{1+\xi} \left\{ \frac{\partial}{\partial r} (\mathbf{F} + \mathbf{V})'' + (\mathbf{H})'' + \epsilon_e \Delta r_i^4 \frac{u_c}{r_c} (\nabla \Delta)^2 \right\} \mathbf{U}'' + \frac{\xi}{1+\xi} \Delta \mathbf{U}''^{-1}. \end{aligned} \quad (24)$$

The operators  $\Delta$  and  $\nabla$  have the conventional definitions:

$$(\Delta)_i f = \frac{f_{i+1} - f_i}{\Delta r_i}, \quad (25a)$$

$$(\nabla)_i f = \frac{f_i - f_{i-1}}{\Delta r_{i-1}}, \quad (25b)$$

so that they indicate forward and backward differences, respectively. The scaling parameters  $r_c$  and  $u_c$  are the radius of the adiabatic (or polytropic) critical point and the adiabatic sound speed at the critical point computed using the base temperature ( $T_0$ ) and defining the critical point in the manner used by Parker (1963):

$$r_c = \frac{GM}{4\gamma RT_0}, \quad (26a)$$

$$u_c = (2\gamma RT_0)^{1/2}. \quad (26b)$$

These definitions are used so that it is not necessary to incorporate any additional scaling in the use of  $\epsilon_i$  and  $\epsilon_e$ .

Fourth order dissipation terms have been added to the explicit portion of (24). This does not impair the formal accuracy of the method. In contrast, second differences operating on  $\Delta \mathbf{U}''$  have been added to the implicit portion of (24). Implicit use of fourth-order differences as dissipation terms would probably produce even wider stability bounds (Steger 1978), but would require block-pentadiagonal matrix inversions of significantly greater complexity. An analysis of the stability bounds on  $\epsilon_e$  and  $\epsilon_i$  has not been made for this specific study. However, Steger (1978) has found that

typically  $\epsilon_s = O[1]$  and  $\epsilon_c = 2.5\epsilon_s$  are upper bounds, but that both terms may be much larger during an impulsive initial start. For the computations done here with the solar wind equations, an attempt has been made to include as little dissipation as possible. Consequently, values of  $\epsilon_s$  and  $\epsilon_c$  have been chosen to be less than or equal to  $2.0 \times 10^{-2}$  for all of the results. Abbreviated studies have shown no effects larger than 1% in timing or magnitude of the profiles for values of either  $\epsilon_s$  or  $\epsilon_c$ , up to at least  $O[1]$ .

#### V. BOUNDARY CONDITIONS

A choice must be made for the boundary conditions to be applied both at the base of the corona—at the first grid point—and at the outer grid point of the computational mesh. For all the examples considered here, the radius of the outer grid point has been chosen such that the flow there is supersonic, and the additional condition is made that the flow be subsonic at the base. Neither of these conditions is necessarily always true for any type of coronal transient, but will be required to be the case here in order to avoid switching the manner in which the boundaries are treated.

An analysis illustrating the mathematically proper method for specifying boundary conditions for time-dependent solutions to the solar wind equations describing adiabatic (or polytropic) flow was presented by Nakagawa and Steinolfson (1976). The application of this and other methods was described by Steinolfson and Nakagawa (1976). The essence of the analysis is (see also Courant and Hilbert 1962) that for a mixed initial boundary value problem only as many boundary conditions can be specified as there are characteristics issuing into the region of interest from that boundary. For the present problem, there are three real characteristics which are related to (i) the flow speed, (ii) the flow speed minus the sound speed, and (iii) the flow speed plus the sound speed. Since the flow is subsonic at the base, the flow speed minus the sound speed is negative, resulting in only two rather than three characteristics issuing into the region of interest. Thus only two dependent variables can be specified at the base of the corona. According to the theory of characteristics, the third dependent variable at the boundary must be determined using some sort of extrapolation depending on the flow variables interior to the boundary.

In the present case, the dependent variables at the inner boundary can be taken as the temperature, density, and velocity, and the choice is made to use temperature and density as the specified boundary variables. It follows now that the velocity at the base must be found using an extrapolation from the interior grid points.

Several methods, in addition to the mathematically "proper method" using the characteristic equations, are examined by Steinolfson and Nakagawa (1976). All of these methods have been tested in the present problem, although the characteristic method was used only for polytropic flow. The most reliable extrapolation from the viewpoint of being able to find the smoothest numerical solutions was simply to let

$$(m_r)_1^n = (m_r)_2^n, \quad (27a)$$

where  $i=1$  and  $i=2$  indicate the grid points at the inner boundary and adjacent to that boundary, respectively, on a grid running from  $i=1$  to  $i=I$ . This extrapolation is exactly true for steady flow, but is only a crude approximation for time-dependent flow that becomes more accurate as the size of the first grid step decreases. The reason this extrapolation works well is that it is the least sensitive to the detailed nature of the profiles and involves only two grid points. Higher order or characteristic method schemes require more complex extrapolations, to which the numerical stability of implicit schemes can be sensitive.

At the outer boundary, the flow is supersonic. In principle, again from characteristic theory, no information can propagate upstream because all characteristic speeds are positive while the region of interest is in the negative direction from the outer boundary. Thus, an extrapolation from the interior flow field profiles must be made for all three of the variables. Here, the very simplest extrapolation is used (see, e.g., BW) by taking

$$U_I^n = U_{I-1}^n, \quad (27b)$$

where  $i=I$  and  $i=I-1$  are the outer boundary and adjacent grid points, respectively. This extrapolation has been found here to be extremely reliable, but the solution can depend on how the temperature gradient at the outer boundary is chosen or computed in finite difference form. This problem will be discussed more in § VI.

Conditions (27a,b) can also be used to advance the boundary conditions to the next time step, giving

$$\Delta U_I^n = \Delta U_{I-1}^n, \quad (28a)$$

$$(\Delta m_r)_1^n = (\Delta m_r)_2^n. \quad (28b)$$

Because  $T_0$  and  $\rho_0$ , the temperature and density at the base, are specified, then

$$\Delta b_1^n = 0, \quad (28c)$$

$$\Delta \epsilon_1^n = \left( \frac{m_r}{b} \right)_1^n (\Delta m_r)_1^n. \quad (28d)$$

This completes the formal statement of the boundary conditions.

The application of (24), together with (27) and (28), at the boundaries of the computation region is best thought of in terms of stepping through the sequence of operations required to advance the solution from time level  $n$  to level  $n+1$ . Consider first the explicit portion of the boundary condition, and then the implicit portion.

#### a) Explicit Portion

The  $i=1$  inner boundary is first encountered for  $i=2$  when inserting the spatial differencing (21a) into the right hand side of (24). Evaluating the derivative  $\partial(F+V)/\partial r$  at  $i=2$  requires values for  $F_1^n$  and  $V_1^n$ . Using (A2) and (13), it is seen that  $F_1^n$  can be determined algebraically in combination with the boundary conditions (27a,b). However,  $V_1^n$  requires an estimate of  $(\partial T/\partial r)_1^n$  which, using (A6g), in turn requires an estimate of  $(\partial b/\partial r)_1^n$ ,  $(\partial m_r/\partial r)_1^n$ , and  $(\partial \epsilon/\partial r)_1^n$ . To find these, the one-sided differences in (22b) are used and the required derivatives at the boundary point are found using  $(b, m_r, \epsilon)_i$  at  $i=1, 2$ , and 3.

Information at the boundary is also required for the dissipation term  $(\nabla \Delta)^2 \mathbf{U}^n$ . To evaluate this fourth-order difference, a centered five-point scheme is invoked in the application of (25a,b). At  $i=2$ , this requires not only information at the  $i=1$  grid point, but also at an imaginary grid point  $i=0$ . The  $i=1$  information is found in the same way as above. The approach used here for the  $i=0$  point is to set  $\mathbf{U}_0^n = \mathbf{U}_1^n$  or, equivalently, to take  $(\nabla) \mathbf{U}_1^n = 0$ . Similarly, at  $i=I-1$  the centered five-point difference used in evaluating the dissipation term requires information at the imaginary grid point  $i=I+1$ . Precisely the same extrapolation is used here as for  $i=2$  such that  $\mathbf{U}_{I+1}^n = \mathbf{U}_I^n$  or  $(\Delta) \mathbf{U}_{I+1}^n = 0$ .

#### b) Implicit Portion

In application of (21a,b) to the left hand side of (24), the three-point central difference scheme results in a now spatially differenced equation of the form (see also [23]):

$$\mathbf{X}_{i-1}^n \Delta \mathbf{U}_{i-1}^n + \mathbf{Y}_i^n \Delta \mathbf{U}_i^n + \mathbf{Z}_{i+1}^n \Delta \mathbf{U}_{i+1}^n = \mathbf{T}_i^n, \quad (29)$$

where

$$\mathbf{X}_{i-1}^n = \frac{\lambda \Delta t}{2 \Delta r_{i-1} (1 + \xi)} \left[ \left( \frac{1}{\Delta r_{i-1}} + \frac{1}{\Delta r_i} \right) \mathbf{P}_{i-1}^n - (\mathbf{A} + \mathbf{C} - \mathbf{P}_r)_{i-1}^n \right] - \frac{1}{\Delta r_{i-1}^2} \epsilon_i \frac{\Delta t}{1 + \xi} \mathbf{I}, \quad (30)$$

$$\mathbf{Y}_i^n = \mathbf{I} + \frac{\lambda \Delta t}{1 + \xi} \left[ \frac{1}{2} \left( \frac{1}{\Delta r_{i-1}} - \frac{1}{\Delta r_i} \right) (\mathbf{A} + \mathbf{C} - \mathbf{P}_r)_i^n - \frac{1}{2} \left( \frac{1}{\Delta r_{i-1}} - \frac{1}{\Delta r_i} \right)^2 \mathbf{P}_i^n + \mathbf{E}_i^n \right] + \left( \frac{1}{\Delta r_i^2} + \frac{1}{\Delta r_{i-1} \Delta r_i} \right) \epsilon_i \frac{\Delta t}{1 + \xi} \mathbf{I}, \quad (31)$$

$$\mathbf{Z}_{i+1}^n = \frac{\lambda \Delta t}{2 \Delta r_i (1 + \xi)} \left[ \left( \frac{1}{\Delta r_{i-1}} + \frac{1}{\Delta r_i} \right) \mathbf{P}_{i+1}^n + (\mathbf{A} + \mathbf{C} - \mathbf{P}_r)_{i+1}^n \right] - \frac{1}{\Delta r_{i-1} \Delta r_i} \epsilon_i \frac{\Delta t}{1 + \xi} \mathbf{I}, \quad (32)$$

$$\mathbf{T}_i^n = -\frac{\Delta t}{1 + \xi} \left\{ \frac{1}{2 \Delta r_{i-1}} \left[ -(\mathbf{F} + \mathbf{V})_{i-1}^n - \left( \frac{\Delta r_{i-1}}{\Delta r_i} - 1 \right) (\mathbf{F} + \mathbf{V})_i^n + \frac{\Delta r_{i-1}}{\Delta r_i} (\mathbf{F} + \mathbf{V})_{i+1}^n \right] + \mathbf{H}_i^n \right\} + \frac{\xi}{1 + \xi} \Delta \mathbf{U}_{i-1}^{n-1}, \quad (33)$$

where  $\mathbf{I}$  = the  $3 \times 3$  identity matrix, and  $\epsilon_i$  is the implicit dissipation coefficient in (24) and is unrelated to the  $i$ -index of the grid point.

For  $i = 2$  and  $i = I - 1$ , the boundaries are encountered in the terms  $X_{i-1}^n \Delta U_{i-1}^n$  and  $Z_{i+1}^n \Delta U_{i+1}^n$ , respectively. At the outer boundary,  $\Delta U_I^n = \Delta U_{I-1}^n$ , from (28a). At the inner boundary, the treatment is slightly more complex.  $\Delta U_1^n$  is found from (28b), (28c), and (28d):

$$\Delta U_1^n = \begin{bmatrix} 0 \\ (\Delta m_r)_2^n \\ \left(\frac{m_r}{b}\right)_1^n (\Delta m_r)_2^n \end{bmatrix}. \quad (34)$$

To incorporate this into (29) it is necessary to write  $X_1^n \Delta U_1^n$  in the form  $X_1^n K_{1B}^n \Delta U_2^n$ . That is:

$$K_{1B}^n \Delta U_2^n = \Delta U_1^n. \quad (35)$$

This is achieved if

$$K_{1B}^n = \begin{bmatrix} 0 & 0 & 0 \\ 0 & 1 & 0 \\ 0 & (m_r/b)_1^n & 0 \end{bmatrix} \quad (36)$$

such that

$$K_{1B}^n \Delta U_2^n = \begin{bmatrix} 0 \\ (\Delta m_r)_2^n \\ (m_r/b)_1^n (\Delta m_r)_2^n \end{bmatrix}. \quad (37)$$

Substitution of (34)–(37) into (29) produces a system of linear equations for  $\Delta U_i^n$ ,  $2 \leq i \leq I - 1$ , which, in matrix form, is

$$\begin{bmatrix} (Y_2 + X_1 K_{1B}) & Z_3 & 0 & & 0 \\ X_2 & Y_3 & Z_4 & & \\ & & & \ddots & \\ 0 & X_{I-3} & Y_{I-2} & Z_{I-1} & \\ & 0 & X_{I-2} & (Y_{I-1} + Z_I) & \end{bmatrix} \begin{bmatrix} \Delta U_2 \\ \Delta U_3 \\ \vdots \\ \Delta U_{I-2} \\ \Delta U_{I-1} \end{bmatrix} = \begin{bmatrix} T_2 \\ T_3 \\ \vdots \\ T_{I-2} \\ T_{I-1} \end{bmatrix} \quad (38a)$$

or

$$Q^n \Delta U^n = T^n, \quad (38b)$$

where  $\Delta U^n$  and  $T^n$  are vectors of dimension  $(I - 2)$  and  $Q^n$  is a block tridiagonal matrix with blocks of dimension  $3 \times 3$ .

The procedure is to compute  $Q^n$  and  $T^n$  for the present time step and to then solve (38) for  $\Delta U^n$ . This gives the increment in the dependent variable for that time step. The new value of the dependent variable at the advance time step is then computed from  $U^{n+1} = U^n + \Delta U^n$ , placing the old value  $U^n$  in an appropriate mass-storage device and replacing it with  $U^{n+1}$  so as to require core memory only for  $\Delta U^n$  and  $U^{n+1}$ . Algorithms for the solution of (38) have been described in many texts such as those by Isaacson and Keller (1966, pp. 58–61) and Varga (1962, pp. 99–102).

#### VI. NUMERICAL RESULTS COMPARING POLYTROPIC AND THERMALLY CONDUCTIVE FLOW

The main example will be a comparison of a transient for thermally conductive flow with a similar transient for polytropic flow. However, before this can be done, the appropriate steady states (that will then be used as initial states for the transient) must be found. This first step is also done using the implicit algorithm in order to demonstrate its use in finding steady-state solutions to the solar wind equations.

In these examples, the mass of the Sun is  $1.989 \times 10^{33}$  g, and the inner boundary radius is  $6.96 \times 10^{10}$  cm. Also, the spatial grid was common for all cases, being described by the formula:

$$\Delta r_{i+1} = \Delta r_i \left( 1 + \frac{\Delta r_{\text{pct}}}{100} \right), \quad I-1 \geq i \geq 1, \quad (39)$$

for  $\Delta r_i \leq \Delta r_{\text{max}}$ , and  $\Delta r_i = \Delta r_{\text{max}}$  at larger radii. In (39),  $\Delta r_i$  is specified, as is  $\Delta r_{\text{pct}}$ , the percent that  $\Delta r_i$  is allowed to increase at each grid step up to its also specified maximum value  $\Delta r_{\text{max}}$ . The maximum radius,  $r_{\text{max}}$ , is prescribed before the grid is computed. Normally, the actual grid would exceed  $r_{\text{max}}$  by some fraction of  $\Delta r_{\text{max}}$  if so allowed. Here, the grid is terminated at the largest radius that is less than  $r_{\text{max}}$  by the latest grid step size. For all the examples,  $\Delta r_i = 0.01 R_{\odot}$ ,  $\Delta r_{\text{pct}} = 10\%$ ,  $r_{\text{max}} = 26 R_{\odot}$ , and  $\Delta r_{\text{max}} = 2.0 R_{\odot}$ . This results in a grid of 59 points spanning  $1.00 R_{\odot}$  to  $25.697 R_{\odot}$ , with the last three steps being the maximum size of  $2.0 R_{\odot}$ . This gives good resolution near the base of the grid, with only 11 grid points lying between  $10 R_{\odot}$  and  $26 R_{\odot}$ .

In the first examples of relaxation from an initial state to the steady state, the initial state will be chosen as isothermal flow for both the polytrope and with thermal conduction. The base temperature and density are  $1.6 \times 10^6$  K and  $7.4 \times 10^7$  cm $^{-3}$ , respectively—the same values chosen by Whang and Chang (1965) in one of the earliest solutions to the steady state solar wind equations with thermal conduction. As described in § II, the thermal conduction description used is the collision-dominated one given by Spitzer (1962) for a fully ionized hydrogen plasma. The polytropic index, gamma, is taken to be 1.10 specifically because this will produce a steady state very nearly the same as that with thermal conduction, between 1.0 and  $21.0 R_{\odot}$ . (If a much larger index were used or required, a Parker-type solution would not exist; see, e.g., Parker 1963, pp. 59ff.)

In these relaxations, the initial state is essentially arbitrary, under the restrictions stated in § V. The boundary conditions are held constant, but the physics is changed at the initial instant. Hence, little physical significance can be attached to the intermediate steps between the initial state and the steady state. The only significance that exists is that the amount of physical time taken to reach the steady state is a reflection of the true amount of time the corona needs, under the prescribed physics, to relax to a steady-state after some perturbation. To minimize the computational time needed to reach the steady state, the time step is allowed to expand in a manner similar to the grid size in (39), except that the time step is allowed to grow only if the profiles are changing no more rapidly than some specified amount anywhere on the grid. In general, the steady states are achieved in physical times of less than 30 hours out to  $20 R_{\odot}$ . This has been found to require about 18 times steps of up to 2.0 hours length in physical time. Comparing this with solutions of the steady state equations, it is analogous to the number of iterations necessary on the location of the critical point in order to match a given temperature and density at the base of the corona. The computational effort for this relatively simple set of equations is very nearly the same in either case (Kopp and Steinolfson, private communication).

The results of the two relaxations are shown in Figure 1, giving the profiles out to  $21 R_{\odot}$ . This is done to absolutely avoid any contamination from the treatment of the outer boundary condition. Curve (i), in each panel, gives the initial state temperature, velocity, and density, respectively. Curves (ii) and (iii) show the resultant steady states for thermally conductive flow and polytropic flow ( $\gamma = 1.10$ ), respectively, after a physical time of 40 hours. As must be the case, these profiles match the known solutions for these boundary conditions, except for small differences in curves (ii) due to the retention of the Coulomb logarithm in the description of thermal conduction, when comparing with the results of Whang and Chang (1965).

It is of some interest from a numerical point of view that these results are produced with no knowledge of the asymptotic nature of the flow profiles at large distances from the Sun and with no reference to critical point nature. It is also notable that no effort was made to choose an initial state near the final state in the relaxations. The steady states were found easily from a distant initial state with time steps that correspond to Courant numbers of up to  $O[10^2 - 10^3]$  even for polytropic flow. As a test of their stability, it is also possible to begin with either curve (ii) or (iii) as an initial state, appropriately change the physics, and relax to curve (iii) or (ii), respectively.

Curves (ii) and (iii) can now be used as initial states for the study of transients. The example that will be shown here invokes an increase in the base temperature from  $1.6 \times 10^6$  K to  $2.0 \times 10^6$  K at  $t = 0$ , and then holds the density and temperature constant thereafter. This impulsive change in the base temperature is not large enough to produce a shock, so a smooth transient in the flow will propagate outwards. As opposed to the above relaxation to find the steady states, the physical description is now constant but the boundary conditions are changed—producing a transient whose properties are of physical interest. The results of this exercise are shown in Figure 2. Figure 2a shows the transient induced on polytropic flow, and Figure 2b shows the same for thermally conductive flow. Profiles are plotted at  $t = 0$ ,

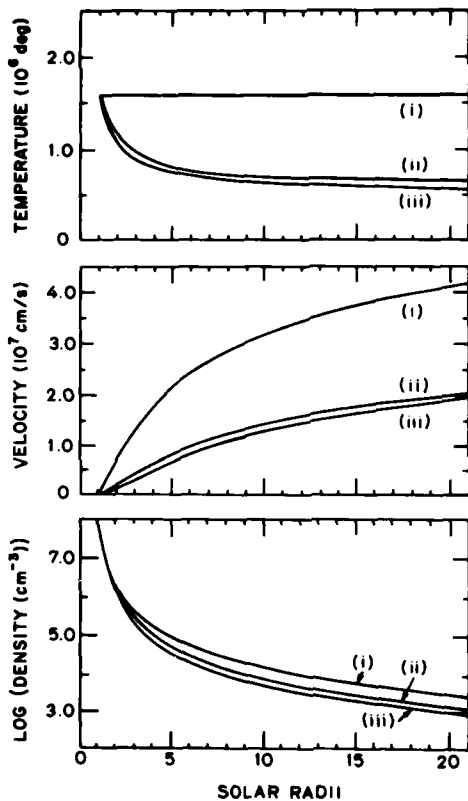


FIG. 1.—(i) Isothermal solar wind flow, used as the initial state for the relaxations to steady states with constant boundary conditions shown as curves (ii) and (iii). (ii) Final state for thermally conductive flow. (iii) Final state for polytropic flow ( $\gamma = 1.10$ ). Both final states are for relaxations times of slightly more than 40 hours.

2, 8, and 20 hours in each case. It is immediately obvious that the two examples produce quite different results even though they begin with similar initial states. Most of these differences are due to the ability of a thermal pulse to propagate at many times the sound speed. However, some of the differences are due to the specific values chosen for the base temperature and density, as will be explained in more detail shortly.

The transient in Figure 2a is, except for its small amplitude, similar to those in, e.g., the model described by Steinolfson and Nakagawa (1976). The initial rise in temperature produces a velocity pulse and compression which is evident in the density profiles. The initial velocity, temperature, and density increases are all in phase because no signal propagates more rapidly than the sound speed. This transient is also very much like transients produced in models limited only to regions of supersonic, polytropic flow. In other words, there is nothing new here, except in comparison between Figures 2a and 2b.

In Figure 2b, it is obvious that the high thermal conductivity allows a thermal pulse to run out in front of the velocity and density transients. In fact, this effect is highly exaggerated because the collisional thermal conductivity used here is not a realistic description of the mid- and outer corona. However, this is not considered to be a deficiency because the primary intent herein is to demonstrate the technique of including thermal conduction and to illustrate comparison of this classical case with polytropic flow. In the transient with thermal conduction, there is an initial temperature rise at all radii after just a few minutes. This temperature rise is seen in the plots of temperature versus time at several different radii in Figure 3. Subsequently, the increased temperature causes a velocity transient to be initiated at the base, much as with the polytrope. This is shown in the velocity profile at a time of 2 hours. At the front of the velocity transient is a compression region which locally increases the temperature. However, unlike in polytropic flow, this local temperature increase is quickly communicated outward to essentially all radii. Behind the compression is a rarefaction that produces a local temperature minimum. In front of the compression the now enhanced temperature causes plasma to begin moving at all radii—a phenomenon which cannot occur for a polytrope, and which corresponds to conductive damping of the principal velocity pulse. Thermal energy has been conducted outward from

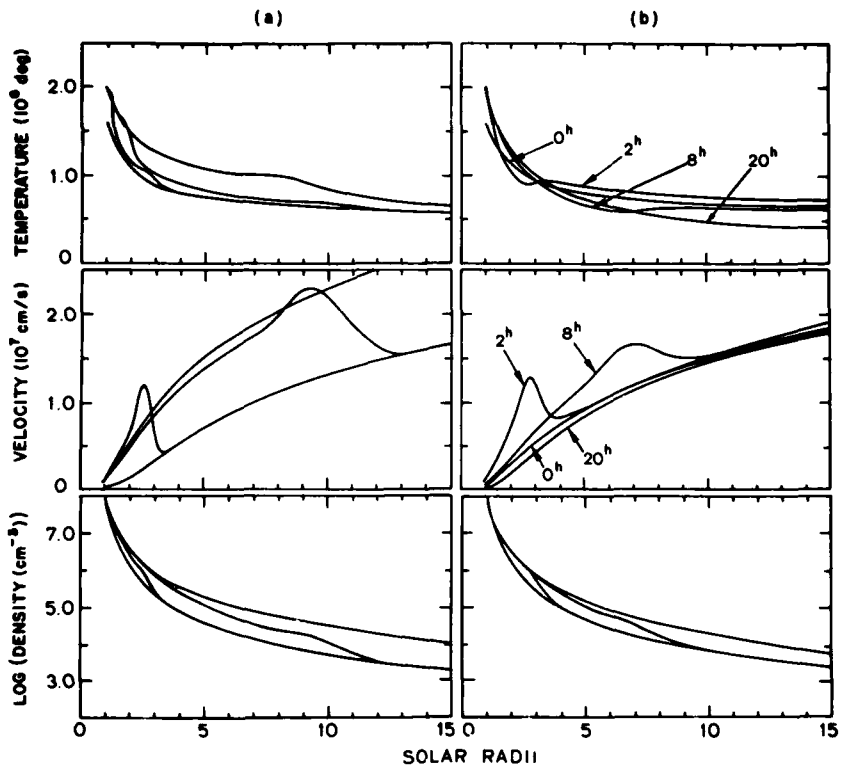


FIG. 2.—The passage of a transient on (a) polytropic flow ( $\gamma = 1.10$ ) and (b) thermally conductive flow. The initial states are those shown as curves (ii) and (iii) in Fig. 1. Profiles are shown at elapsed time of 0, 2, 8, and 20 hours in all cases. The transient was introduced by instantaneously increasing the base temperature from  $1.6 \times 10^6$  to  $2.0 \times 10^6$  K at  $t = 0$ , and holding the temperature and density at the base constant at all later times. Unlike Fig. 2a, the final state in Fig. 2b has a flow velocity lower than the initial state. This effect is due to the particular choice of base temperatures and density for the thermally conductive flow, and enhances the apparent differences between Figs. 2a and 2b.

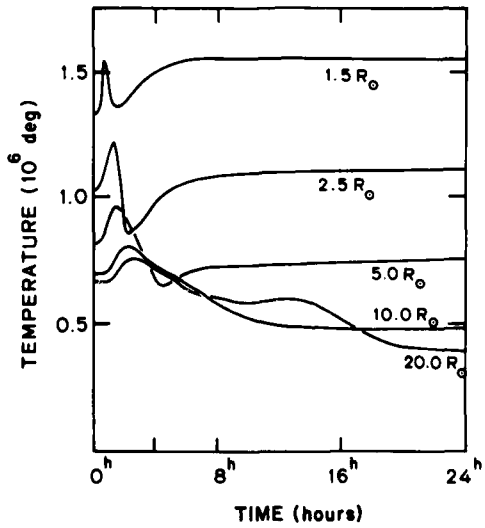


FIG. 3.—The time variation of the temperature at 1.5, 2.5, 5.0, 10.0, and 20.0 solar radii for the example of a transient in thermally conductive flow shown in Fig. 2b.

the principal velocity pulse and is being partially converted to bulk motion. The density transient is similar to the transient for polytropic flow, although the differences are deemphasized in this logarithmic plot.

At later times the differences between Figure 3a and 3b are just an extension of the above description. In addition, the pathological nature of the initial choice of boundary conditions for thermally conductive flow becomes evident. In Figure 3b, the velocity at 20 hours is seen to be lower than the initial velocity. This is a real effect in that for the specified base temperature and density, a slight increase in the base temperature will result in a lower velocity at 1 AU and at all radii out to 1 AU, as described by Holzer and Leer (1981). This is radically different from the case for polytropic flow, which produces increased velocities for increased base temperatures in all cases. A significant portion of the difference in velocity profiles between Figures 3a and 3b must be attributed to this effect.

This pathological effect can be suppressed by choosing initial and final base temperatures and densities that result in similar initial and final profiles for both polytropic and thermally conductive flow. Because the problem is highly nonlinear, this suppression is not entirely possible. However, a good approximation to such a case is shown in Figure 4. Here, the base density has been chosen to be a lower value of  $1.0 \times 10^7 \text{ cm}^{-3}$ , while the initial and final base temperatures are the same as in Figure 2. Inspection of Figure 1 from Holzer and Leer (1981) shows this choice of parameters to result in increasing velocities with increasing base temperature and thermal conduction. The initial and final profiles are quite similar, although not identical. The results for a polytrope are shown in Figure 4a and for thermally conductive flow in Figure 4b. Profiles are plotted at  $t = 0, 2, 5, 10$  hours in Figure 4b. In Figure 4a, an additional profile at  $t = 20$  hours is plotted because it was found that it took longer for the polytrope flow to reach an apparent steady state. Although the time of arrival of the transient is slightly different, the qualitative nature of the transient on polytropic flow is the same as in Figure 2. For conductive flow, there are some large differences between this case and the case shown in Figure 2—as was expected. The two most striking differences are that the magnitude of

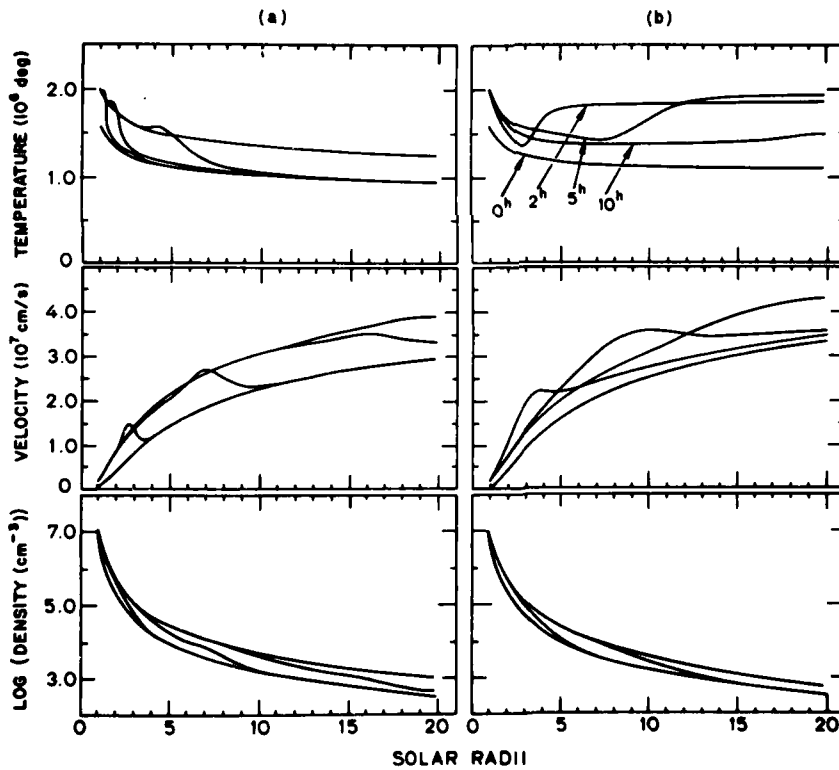


FIG. 4.—The passage of a transient on (a) polytropic flow ( $\gamma = 1.05$ ) and (b) thermally conductive flow. The initial states have the same base temperature as curve (ii) and (iii) in Fig. 1, but the base densities are now  $1.0 \times 10^7 \text{ cm}^{-3}$  rather than  $7.4 \times 10^7 \text{ cm}^{-3}$ . Profiles are shown at elapsed times of 0, 2, 5, and 10 hours in Fig. 4b, and at the same times plus at 20 hours in Fig. 4a because the polytropic flow relaxes more slowly to a steady state than does the thermally conductive flow. The transient was again introduced by instantaneously increasing the base temperature from  $1.6 \times 10^6$  to  $2.0 \times 10^6 \text{ K}$  at  $t = 0$ , and holding the temperature and density at the base constant at all late times. In addition to the initial states, the final state in Fig. 4a is now similar to the final state in Fig. 4b. The differences between the two examples are primarily due to the ability of a thermal pulse to propagate out in front of the velocity pulse in Fig. 4b.

the temperature rise in front of the compression region is much larger and that the velocity pulse is much smoother and more spread out. These differences are due to the overall lower density in the corona and the corresponding higher thermal conductivity, causing a significant shift in the energy distribution and propagation. What is more important is that this figure demonstrates the important effects of thermal conduction on the propagation of a transient in the corona, in comparison to a similar transient in a polytropic gas. The initial and final steady states are very close for the two opposing cases, so the differences represent a realistic picture of these effects.

It is possible to view the results shown in Figure 4b in a slightly different manner. Because the heat pulse propagates outward in front of the velocity transient at the expense of the energy in the velocity transient, the net effect is extraction of energy from some instantaneous state low in the corona and deposition of that energy in the mid- and outer corona. In a sense, the passage of the velocity pulse has a refrigerating effect on the low corona. This is only a transient effect, so it does not necessarily represent any average heating of the outer corona or cooling of the inner corona, although such could be the case in the presence of a continuous wave train.

The last two examples that will be shown are the result of an investigation of the effect of alternate treatment of the outer boundary condition. The results shown in Figures 1-4 used the condition given in (27b). From (14), this would seem to suggest that  $(\partial T / \partial r)_I$ , the temperature gradient at the last grid point, is zero. However, this is not necessarily the case, depending on how derivatives are constructed in finite difference form. In the previous examples, derivatives at  $i = I$  were constructed using the three-point one-sided form given in (22a) which, when combined with (27b), results in a value for the temperature gradient at the outer grid point that is approximately half the gradient at the next point inward. That is,

$$\left( \frac{\partial T}{\partial r} \right)_I \approx \frac{1}{2} \left( \frac{\partial T}{\partial r} \right)_{I-1}. \quad (40)$$

The general requirement, physically, is that the outer boundary condition on the temperature gradient should allow

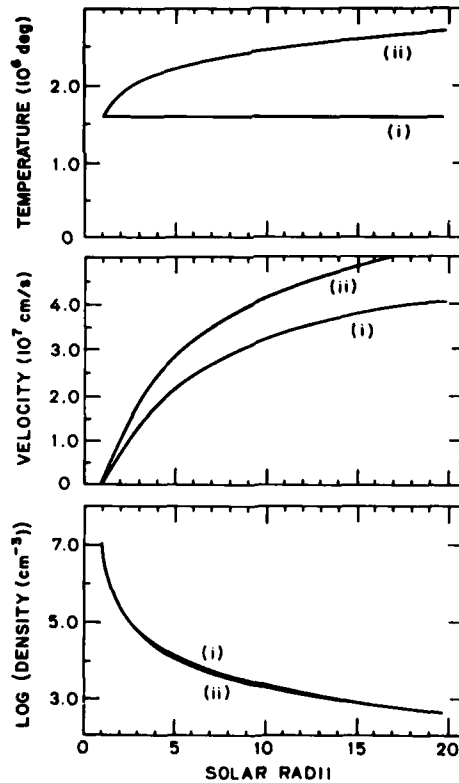


FIG. 5.—At attempt to find a steady state from an initial state of identical to curve (i) in Fig. 1. Here, however, the boundary condition at the outer boundary was altered to make the temperature gradient as computed between the  $i = I$  and  $i = (I - 1)$  grid points equal that between the  $i = (I - 1)$  and  $i = (I - 2)$  grid points. Curves (i) show the initial state, and curves (ii) show the profiles after 23 hours. These profiles continue to diverge from the known final steady state with time.

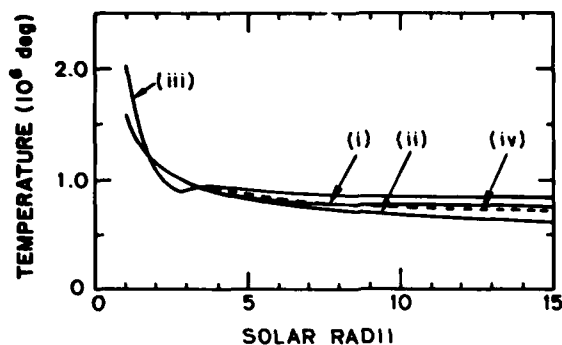


FIG. 6.—Temperature variation for a transient on thermally conductive flow two hours after the temperature at the base was impulsively increased from  $1.6 \times 10^6$  to  $2.0 \times 10^6$  K. The base density is  $7.4 \times 10^7 \text{ cm}^{-3}$ . Two initial states, curves (i) and (ii), have been used. Curve (i) is the same initial state shown in Fig. 1b. Curve (ii) is the same as (i) except with outer boundary condition as in Fig. 5. Here, a relaxation, using curve (i) as an initial state, did produce the new steady state (ii) with slightly lower temperatures near the outer boundary. The two transients seem similar, in spite of the modified boundary condition. This will not be the case as the transient approaches the boundary of the computation region.

heat to conduct through the boundary in as natural a manner as possible. Alternate treatment of the finite differencing at  $i = I$  can greatly affect how well this requirement is met, regardless of the physical treatment of the boundary condition. It can be shown analytically that nearby values of  $\partial T / \partial r$  to that given in (40) do not greatly affect the solution. The largest effects are found, in any case, near the boundary and when variables are rapidly changing near the boundary. What cannot be done is to change the sign of either the slope of the temperature gradient as computed using the points  $i = I$  and  $i = I - 1$ , or of the curvature as computed using the points  $i = I, I - 1$ , and  $I - 2$ . Thus, choosing to evaluate  $\partial T / \partial r$  using only  $i = I$  and  $i = I - 1$ , together with the boundary condition (27b), would usually cause erroneous results because the slope has been changed from a negative value to zero. Similarly, choosing  $(\partial T / \partial r)_i = (\partial T / \partial r)_{i-1}$  would cause the curvature at the outer grid point to be computed as zero. The results of this second choice are what are shown in Figures 5 and 6.

The choice that  $(\partial T / \partial r)_i = (\partial T / \partial r)_{i-1}$  might be expected to be a reasonable alternative to the extrapolation (40). In fact, an extrapolation similar to (27b) could be invoked which would give exactly this temperature gradient when applying (22a). Physically, however, this choice represents an extreme enhancement of the manner in which heat is conducting through the outer boundary. If the temperature gradient is too steep, then (i) more heat will conduct out past the last grid point than should, (ii) temperatures in the vicinity of the boundary will be too low, and (ii) velocities will be locally increased. Conversely (and by far a worse situation), if the temperature gradient at the outer boundary becomes positive during a transient, then the boundary appears as a heat source under the above extrapolation of the temperature gradient. This heat source at the outer boundary apparently then never disappears at later times. Such a case is shown in Figure 5, where a relaxation from isothermal flow to a steady state was attempted using precisely the same parameters as in Figure 1 for a relaxation with thermal conduction (relaxation from profiles [i] to [iii] in Fig. 1). In Figure 5, the initial isothermal flow is given by curves (i), and the profiles after 23 hours physical time are shown by curves (ii). The temperature has risen above the isothermal state, and is continuing to rise at all radii because at the initial time step the flow was hotter than in the steady state and so was compressed slightly near the outer boundary. This compression raised the temperature slightly at the outer boundary, causing the temperature gradient there to become positive. The consequence is as described above. The outer boundary now acts as a heat source, the temperature and velocity are too large, and a steady state is not being approached.

A contrasting situation is shown in Figure 6. Here only the temperature is plotted for two different cases, at time  $t = 0$  and  $t = 2$  hours. The initial state (i) is the same as in Figure 2b. This initial state was then used in two ways. First, a transient was introduced by increasing the base temperature from  $1.6 \times 10^6$  K to  $2.0 \times 10^6$  K, with the resulting temperature profile after 2 hours being shown by curve (iii). Next, (i) was used to generate a new steady state with the alternate extrapolation for the temperature gradient at the outer boundary that was used for the results shown in Figure 5. In the present case, the temperature gradient at  $i = I$  never becomes positive, and a new steady state is achieved with slightly depressed temperatures near the outer boundary—shown by curve (ii). Then curve (ii), and the associated velocity and density, were used as the initial state for another transient that was introduced again by increasing the temperature from  $1.6 \times 10^6$  to  $2.0 \times 10^6$  K. The temperature profiles after 2 hours are shown by curve (iv), which is essentially identical to curve (ii) out to  $3.5 R_\odot$ . This example shows that the extreme choice for extrapolating the temperature gradient at the outer boundary does not greatly affect flow properties as long as the

temperature gradient does not become positive at that boundary. However, eventually the transient shown by curve (iv) will reach the boundary, causing a reversal in the sign of the temperature gradient. Subsequent evolution of the transient with this boundary condition will continue to diverge from the physical solution due to the same effect demonstrated in Figure 5.

These last two examples were meant to demonstrate the physical limitations on extrapolation such as (27b) in combination with finite difference approximations at the boundaries. As long as these physical limitations are not violated, it is possible to show analytically that other extrapolations of the temperature gradient than that chosen here only have small effect on the solution, and then only in the vicinity of the boundary.

#### VII. USE OF THIS ALGORITHM IN SOLAR AND STELLAR WIND STUDIES

Many processes can already be modeled with the algorithm described in §§ III-V, including propagation and conductive damping of waves and wave trains that are any combination of temperature, velocity, and density variation at the base. In addition, alternate forms for thermal conduction in the context of single fluid equations can be investigated, including use of a term derived from a table look-up as opposed to a purely analytical form. However, there are important and obvious deficiencies in the use of equations (1)-(3) to describe solar and stellar winds. The most important stellar winds are radiatively driven, and will be discussed below. For the solar wind, several additions to these equations might be of interest, so a brief outline of how to go about some such additions will be given here.

Many of the interesting additions to the solar wind equations take the form of source (or loss) terms in the energy and momentum equations. These terms are a consequence of the inference that energy and momentum addition are important in the corona above the transition region (Suess *et al.* 1977; Holzer 1977). It is uncertain what dependence these terms have on the conserved variables, so here arbitrary functions will be assumed. These additions would have the effect of modifying the  $\mathbf{H}$ -vector (eqs. [15] and [A4]) to give

$$\mathbf{H} = \begin{bmatrix} 0 \\ -2rp + bGM/r^2 - r^2q_w \\ m,GM/r^2 - r^2q_e \end{bmatrix}. \quad (41)$$

So far, this does not complicate things much, but it does further remove the system of equations from purely conservation form. The additional complexity comes in evaluation of the nonlinearities in  $\mathbf{H}$  for evaluation at the advance time step, or in construction of the Jacobian matrix  $\mathbf{E}$  (eq. [19c]). In addition to  $\mathbf{E}$ , there must be one new Jacobian matrix,  $\mathcal{K}$ , because  $q_w$  and  $q_e$  may depend on  $\mathbf{U}$ . This introduces the following two matrices:

$$\mathcal{K} = \frac{\partial \mathbf{H}}{\partial \mathbf{U}}, \quad (42a)$$

$$\mathcal{K}_r = \frac{\partial \mathcal{K}}{\partial r}, \quad (42b)$$

into appropriate places in equation (20) or (24).

The additional terms shown in (41) and (42) in solar wind studies suggest many new avenues of research. One example will be suggested involving a question of the stability of a solution to the equivalent steady-state equations. Finding steady state solutions with totally ad hoc terms such as  $q_w$  and  $q_e$  has been done by Leer and Holzer (1981), but (as they point out) certain solutions involving an inferred standing shock transition from subsonic to supersonic flow in the fluid frame, in the presence of extended heat and momentum addition, may not be steady. This stability question can be answered through a relaxation analysis such as described in connection with Figure 1, with the above additions to the equations.

The other important addition to the original equations that might be suggested for one-dimensional solar wind studies is the extension to two-fluid or multiple-fluid flow. This requires additional equations for the additional ion species. The algebraic complexity is somewhat greater for such models and the dimensions of the vectors and matrices all increase by at least one for each additional species.

For stellar winds, the driving force for those that can be directly observed is not the pressure gradient, as with the solar wind, but rather radiation pressure. This force can be parameterized as being approximately proportional to the

local velocity gradient (Castor, Abbott, and Klein 1975), and thus incorporated into a formulation like that outlined above in (41) and (42). This allows direct numerical modeling of steady and transient flow in radiatively driven winds. Furthermore, the functional relationships in (41) and (42) need not be analytic. Just as with thermal conduction, it is completely possible to use a table look-up to determine the radiative force for any combination of the variables. This, in fact, is probably the preferred approach for stellar winds as the parameterization of Castor, Abbott, and Klein is valid for only a relatively small region of parameter space (Abbott, personal communication).

In principle, generalization of the boundary conditions described in § V would allow an even broader treatment of winds. By initially specifying a hydrostatic stratification and dropping the pressure at the outer boundary to a very low value at  $t = 0$ , it should be possible to study stellar wind startup. This has been done already for isothermal flow (Kopp, personal communication) and is a problem of great interest. The opposite problem of stellar wind quenching, although probably of less interest, could be addressed in an analogous manner.

The intent in this section has been to outline the mechanics of applying the algorithm described in §§ III-V to different problems. Other examples than those given above can be imagined, but most of the necessary tools for any possible example are included in the above discussion. This does not include extension to more than one spatial dimension. However, multidimensional flow is discussed in great detail by BW.

#### VIII. SUMMARY

The time-dependent solar wind equations, including thermal conduction, present a particularly difficult problem in their numerical solution due their being extremely "stiff"—resulting in the Courant stability condition present with all explicit time-difference schemes requiring such small time steps for numerical stability that it is generally not feasible to include thermal conduction. Here a detailed description has been given of a general implicit time-difference scheme that completely avoids the above stability condition. The algorithm is mathematically concise and is found to be computationally efficient. Other than the algebraic complexity present in all implicit schemes, the primary area in which problems might occur with this algorithm is in the treatment of the boundary conditions. A special effort has been made to identify particular problems and solutions in dealing with the boundary conditions for varying cases.

A specific model is described involving flow which is subsonic at the inner boundary and supersonic at the outer boundary of the computation region. These boundary condition choices are made because this is the simplest case to deal with. However, any other choice can be implemented while still using the BW algorithm. The model is then first used to find steady-state solutions through a relaxation in time from some arbitrarily chosen initial state while holding the boundary values of the temperature and density constant. The steady state is found with computational times comparable to those required to solve the steady-state equations alone. It is anticipated that any additions to the physical processes included in the equations of motion would result in the relaxation being the most efficient way, computationally, to produce steady-state solutions.

The model is next used to give examples comparing the passage of a transient on polytropic flow with the passage of a similar transient on thermally conductive flow. This is done for (i) initial states similar to each other and boundary conditions identical to those chosen by Whang and Chang (1965) in a very early solution to the solar wind equations with thermal conduction, and (ii) similar initial states with somewhat lower base densities than in the first case, which also results in similar final states after the base temperature has been instantaneously increased to introduce the transient. Large differences are shown to exist. These differences are primarily due to the ability of a heat pulse to propagate at many times the sound speed.

Application of the algorithm to different problems and improvements to the model to better describe the physics are briefly outlined so as to provide the necessary guidance in order to apply the techniques described here to different problems.

I would like to thank Professor John Wilcox for a generous invitation to visit the Institute for Plasma Research for the 1980-1981 academic year for the purpose of developing the present numerical model. While visiting Stanford University, I also received considerable help from Phil Scherrer and Josh Knight. I would also like to thank Professor Joe Steger, who gave valuable advice whenever I came to a point beyond which my own limited knowledge of numerical techniques could not carry me. Finally, I would like to thank the referee for very helpful comments on several details.

This work was supported in part by the Office of Naval Research under contract N00014-76-C-0207, by the National Aeronautics and Space Administration under grant NGR 05-020-559 and contract NASS-24420, by the Division of Atmospheric Sciences, Solar Terrestrial Research Program of the National Science Foundation under grant ATM77-20580, by the Max C. Fleischmann Foundation, and by the National Center for Atmospheric Research, which is sponsored by the National Science Foundation, for computer time used in this research.

## APPENDIX

For the solar wind equations written in matrix form (eq. [15]), the vector of conserved variables  $\mathbf{U}$ , the flux vectors  $\mathbf{F}$  and  $\mathbf{V}$ , and the vector of inhomogeneous terms are

$$\mathbf{U} = \begin{bmatrix} \rho r^2 \\ \rho v_r r^2 \\ \left( \frac{\rho}{\gamma-1} + \frac{1}{2} \rho v_r^2 \right) r^2 \end{bmatrix} \equiv \begin{bmatrix} b \\ m_r \\ \epsilon \end{bmatrix}, \quad (\text{A1})$$

$$\mathbf{F} = \begin{bmatrix} m_r \\ \frac{m_r^2}{b} + r^2 p \\ \frac{m_r}{b} (\epsilon + r^2 p) \end{bmatrix}, \quad (\text{A2})$$

$$\mathbf{V} = \begin{bmatrix} 0 \\ 0 \\ -r^2 \kappa \frac{\partial T}{\partial r} \end{bmatrix}, \quad (\text{A3})$$

$$\mathbf{H} = \begin{bmatrix} 0 \\ -2rp + b \frac{GM}{r^2} \\ m_r \frac{GM}{r^2} \end{bmatrix}, \quad (\text{A4})$$

where  $p$  is the gas pressure (eq. [13]),  $T$  is the temperature (eq. [14]), and  $\kappa$  is the coefficient of thermal conduction (eqs. [6]–[8]). Using these vectors, the Jacobian matrices  $\mathbf{A}$ ,  $\mathbf{C}$ ,  $\mathbf{E}$ ,  $\mathbf{P}$ , and  $\mathbf{P}_r$ , defined in (19), are

$$\mathbf{A} = \frac{\partial \mathbf{F}}{\partial \mathbf{U}} = \begin{bmatrix} 0 & 1 & 0 \\ \frac{\gamma-3}{2} \left( \frac{m_r}{b} \right)^2 & (3-\gamma) \frac{m_r}{b} & \gamma-1 \\ \left( \frac{m_r}{b} \right)^2 \left( \frac{\gamma-1}{b} m_r^2 - \gamma \epsilon \right) & \frac{1}{b} \left( \gamma \epsilon - \frac{3}{2} (\gamma-1) \frac{m_r^2}{b} \right) & \gamma \frac{m_r}{b} \end{bmatrix}, \quad (\text{A5})$$

$$\mathbf{C} = \frac{\partial \mathbf{V}}{\partial \mathbf{U}} = -r^2 \begin{bmatrix} 0 & 0 & 0 \\ 0 & 0 & 0 \\ \left( \frac{\partial \kappa}{\partial b} \frac{\partial T}{\partial r} + \kappa \frac{\partial^2 T}{\partial r \partial b} \right) & \left( \frac{\partial \kappa}{\partial m_r} \frac{\partial T}{\partial r} + \kappa \frac{\partial^2 T}{\partial r \partial m_r} \right) & \left( \frac{\partial \kappa}{\partial \epsilon} \frac{\partial T}{\partial r} + \kappa \frac{\partial^2 T}{\partial r \partial \epsilon} \right) \end{bmatrix}, \quad (\text{A6})$$

in which

$$\frac{\partial \kappa}{\partial b} = \frac{\kappa_0 T^{3/2}}{2 \ln \Lambda} \left[ \left( 5 - \frac{3}{\ln \Lambda} \right) \frac{\partial T}{\partial b} + \frac{T}{b \ln \Lambda} \right], \quad (\text{A6a})$$

$$\frac{\partial \kappa}{\partial m_r} = \frac{\kappa_0 T^{3/2}}{2 \ln \Lambda} \left( 5 - \frac{3}{\ln \Lambda} \right) \frac{\partial T}{\partial m_r}, \quad (\text{A6b})$$

$$\frac{\partial \kappa}{\partial \epsilon} = \frac{\kappa_0 T^{3/2}}{2 \ln \Lambda} \left( 5 - \frac{3}{\ln \Lambda} \right) \frac{\partial T}{\partial \epsilon}. \quad (\text{A6c})$$

$$\frac{\partial^2 T}{\partial r \partial b} = \frac{\gamma-1}{2 R b^3} \left[ \left( 2\epsilon - \frac{3m_r^2}{b} \right) \frac{\partial b}{\partial r} + 2m_r \frac{\partial m_r}{\partial r} - b \frac{\partial \epsilon}{\partial r} \right], \quad (\text{A6d})$$

$$\frac{\partial^2 T}{\partial r \partial m_r} = \frac{\gamma-1}{2 R b^3} \left( \frac{2m_r}{b} \frac{\partial b}{\partial r} - \frac{\partial m_r}{\partial r} \right), \quad (\text{A6e})$$

$$\frac{\partial^2 T}{\partial r \partial \epsilon} = -\frac{\gamma-1}{2 R b^2} \frac{\partial b}{\partial r}, \quad (\text{A6f})$$

$$\frac{\partial T}{\partial r} = \frac{\gamma-1}{2 R b} \left[ \left( \frac{m_r^2}{b} - \epsilon \right) \frac{1}{b} \frac{\partial b}{\partial r} + \frac{\partial \epsilon}{\partial r} - \frac{m_r}{b} \frac{\partial m_r}{\partial r} \right], \quad (\text{A6g})$$

$$\mathbf{E} = \frac{\partial \mathbf{H}}{\partial \mathbf{U}} = \begin{bmatrix} 0 & 0 & 0 \\ \left( -\frac{\gamma-1}{R b^2} m_r^2 + \frac{GM}{r^2} \right) & \frac{2(\gamma-1)}{br} m_r & -\frac{2(\gamma-1)}{r} \\ 0 & \frac{GM}{r^2} & 0 \end{bmatrix}, \quad (\text{A7})$$

$$\mathbf{P} = \frac{\partial \mathbf{V}}{\partial \mathbf{U}_r} = -r^2 \kappa \begin{bmatrix} 0 & 0 & 0 \\ 0 & 0 & 0 \\ \frac{\partial^2 T}{\partial r \partial b_r} & \frac{\partial^2 T}{\partial r \partial m_{r,r}} & \frac{\partial^2 T}{\partial r \partial \epsilon_r} \end{bmatrix} \quad (\text{A8})$$

in which

$$b_r = \frac{\partial b}{\partial r}, \quad (\text{A8a})$$

$$m_{r,r} = \frac{\partial m_r}{\partial r}, \quad (\text{A8b})$$

$$\epsilon_r = \frac{\partial \epsilon}{\partial r}, \quad (\text{A8c})$$

$$\frac{\partial^2 T}{\partial r \partial b_r} = \frac{\gamma-1}{2 R b^2} \left( \frac{m_r^2}{b} - \epsilon \right), \quad (\text{A8d})$$

$$\frac{\partial^2 T}{\partial r \partial m_{r,r}} = -\frac{(\gamma-1)}{2 R b^2} m_r, \quad (\text{A8e})$$

$$\frac{\partial^2 T}{\partial r \partial \epsilon_r} = \frac{\gamma-1}{2 R b}, \quad (\text{A8f})$$

$$\mathbf{P}_r = \frac{\partial \mathbf{P}}{\partial r} = -r^2 \kappa \begin{bmatrix} 0 & 0 \\ 0 & 0 \\ \left( \frac{2}{r} \frac{\partial^2 T}{\partial r \partial b_r} + \frac{1}{\kappa} \frac{\partial \kappa}{\partial r} \frac{\partial^2 T}{\partial r \partial b_r} + \frac{\partial^3 T}{\partial r \partial b_r \partial r} \right) & \left( \frac{2}{r} \frac{\partial^2 T}{\partial r \partial m_{r,r}} + \frac{1}{\kappa} \frac{\partial \kappa}{\partial r} \frac{\partial^2 T}{\partial r \partial m_{r,r}} + \frac{\partial^3 T}{\partial r \partial m_{r,r} \partial r} \right) \\ & \left( \frac{2}{r} \frac{\partial^2 T}{\partial r \partial \epsilon_r} \frac{1}{\kappa} \frac{\partial \kappa}{\partial r} \frac{\partial^2 T}{\partial r \partial \epsilon_r} + \frac{\partial^3 T}{\partial r \partial \epsilon_r \partial r} \right) \end{bmatrix}, \quad (\text{A9})$$

in which equations (A8c,d,e,f) are used in the evaluation, along with

$$\frac{\partial \kappa}{\partial r} = \kappa \left[ \left( 5 - \frac{3}{\ln \Lambda} \right) \frac{1}{2T} \frac{\partial T}{\partial r} + \frac{1}{2 \ln \Lambda} \left( \frac{1}{b} \frac{\partial b}{\partial r} - \frac{2}{r} \right) \right], \quad (A9a)$$

$$\frac{\partial^3 T}{\partial r \partial b, \partial r} = \frac{\gamma-1}{2Rb^3} \left[ 2m_r \frac{\partial m_r}{\partial r} - \left( \frac{3m_r^2}{b} - 2\epsilon \right) \frac{\partial b}{\partial r} - b \frac{\partial \epsilon}{\partial r} \right], \quad (A9b)$$

$$\frac{\partial^3 T}{\partial r \partial m_r, \partial r} = \frac{\gamma-1}{2Rb^3} \left( 2m_r \frac{\partial b}{\partial r} - b \frac{\partial m_r}{\partial r} \right), \quad (A9c)$$

$$\frac{\partial^3 T}{\partial r \partial \epsilon, \partial r} = - \frac{(\gamma-1)}{2Rb^2} \frac{\partial b}{\partial r}. \quad (A9d)$$

## REFERENCES

Beam, R. M., and Warming, R. F. 1976, *J. Comput. Phys.*, **22**, 87.  
 ———, 1978, *AIAA J.*, **16**, 393 (BW).

Briley, W. R., and McDonald, H. 1975, *Proc. Fourth Internat. Conf. on Numer. Meth. in Fluid Dyn., Lecture Notes in Physics*, Vol. 35 (Berlin: Springer-Verlag), pp. 105-110.

Castor, J. I., Abbott, D. C., and Klein, R. I. 1975, *Ap. J.*, **195**, 157.

Courant, R., and Hilbert, D. 1962, *Methods of Mathematical Physics*, Vol. 2, *Partial Differential Equations* (New York: Interscience).

Craig, I. J. D., and McClymont, A. N. 1976, *Solar Phys.*, **50**, 133.

Dwyer, H. A. 1981, *Annual Rev. Fluid Mech.*, **13**, 217-229.

Han, S. M., Wu, S. T., and Nakagawa, Y. 1981, *Computers and Fluids*, in press.

Harlow, F. H. (ed.) 1973, *Computer Fluid Dynamics — Recent Advances (AIAA Selected Reprint Series, Vol. 15)*.

Holzer, T. E. 1977, *J. Geophys. Res.*, **82**, 23.

Holzer, T. E., and Leer, E. 1981, *J. Geophys. Res.*, **85**, 4665.

Hundhausen, A. J., and Gentry, R. A. 1969, *J. Geophys. Res.*, **74**, 6229.

Isaacson, E., and Keller, H. B. 1966, *Analysis of Numerical Methods* (New York: Wiley).

Leer, E., and Holzer, T. E. 1981, *J. Geophys. Res.*, **85**, 4681.

Lindemuth, I., and Kileen, J. 1973, *J. Comput. Phys.*, **13**, 181.

Metzler, N., Cuperman, S., Dryer, M., and Rosenau, P. 1979, *Ap. J.*, **231**, 960.

Nakagawa, Y., and Steinolfson, R. S. 1976, *Ap. J.*, **207**, 296.

Parker, E. N. 1963, *Interplanetary Dynamical Processes* (New York: Interscience).

Pizzo, V. J. 1980, *J. Geophys. Res.*, **85**, 727.

Richtmyer, R. D., and Morton, R. D. 1967, *Difference Methods for Initial Value Problems* (New York: Interscience).

Schnack, D. 1978, Ph.D. thesis, Dept. of Applied Physics, University of California at Davis.

Spitzer, L., Jr. 1962, *Physics of Fully Ionized Gases* (New York: Interscience).

Steger, J. L. 1978, *AIAA J.*, **16**, 679.

Steger, J. L., and Bailey, H. E. 1980, *AIAA J.*, **18**, 249.

Steinolfson, R. S., Dryer, M., and Nakagawa, Y. 1975, *J. Geophys. Res.*, **80**, 1223.

Steinolfson, R. S., and Nakagawa, Y. 1976, *Ap. J.*, **207**, 300.

Suess, S. T., Richter, A. K., Winge, C. R., and Nerney, S. R. 1977, *Ap. J.*, **217**, 296.

Varga, R. S. 1962, *Matrix Iterative Analysis* (Englewood Cliffs: Prentice-Hall).

Whang, Y. C., and Chang, C. C. 1965, *J. Geophys. Res.*, **70**, 4175.

Wu, S. T., Kan, L. C., Nakagawa, Y., and Tandberg-Hanssen, E. 1981, *Solar Phys.*, **70**, 137.

S. T. SUESS: Space Environment Laboratory, NOAA/ERL, 325 Broadway, Boulder, CO 80303

# Helium Abundance Enhancements in the Solar Wind

G. BORRINI

*Institute for Plasma Research, Stanford University, Stanford, California 94305*

J. T. GOSLING, S. J. BAME, AND W. C. FELDMAN

*Los Alamos National Laboratory, Los Alamos, New Mexico 87544*

Helium abundance ( $A(He)$ ) enhancements observed with Los Alamos instruments on IMP 6, 7, and 8 during the 1972-1978 interval have been investigated. Statistical analysis of 73 large events with  $A(He) \geq 10\%$  (HAEs) provides evidence for a close link between helium enhancements at 1 A.U. and transient coronal mass ejections. HAE events are sporadic, sometimes clustered in time, and their frequency of occurrence is approximately in phase with the solar cycle. Nearly 50% of HAEs are associated with interplanetary shocks and/or geomagnetic activity sudden commencements, but the plasma pattern associated with  $A(He)$  enhancements is independent of shock occurrence. This pattern features high magnetic field strength, low alpha-proton velocity difference, and low proton temperature. These plasma properties suggest that the enhancement is embedded in a 'closed,' magnetically dominated structure that expands adiabatically. In fact, HAEs are likely to be still evolving dynamically at 1 A.U. Evidence of a significant association between helium enhancements at 1 A.U. and type II and IV radio bursts in the corona is presented. We interpret these results to mean that most HAE events originate in transient coronal disturbances in which the magnetic field strength is enhanced.

## 1. INTRODUCTION

Helium abundance with respect to hydrogen (hereinafter referred as  $A(He)$ ) is a parameter that varies greatly within the solar wind at 1 A.U. Measurements collected in situ over the last 15 years [e.g., Neugebauer and Snyder, 1966; Robbins et al., 1970; Ogilvie and Wilkerson, 1969; Bame, 1972; Bollea et al., 1972; Feldman et al., 1977; Neugebauer, 1981] indicate that the solar wind  $A(He)$  varies from less than 0.001 to greater than 0.35. Such variability was not expected a priori and has received considerable attention since its discovery, both theoretically [e.g., Jokipii, 1966; Nakada, 1969; Joselyn and Holzer, 1978; Geiss et al., 1970; Hollweg et al., 1978; Borrini and Noci, 1979; Hollweg, 1981; Kopp et al., 1981] and observationally [e.g., Hirshberg et al., 1972a, b, 1974; Ogilvie, 1972; Moreno and Palmiotti, 1973; Ogilvie and Hirshberg, 1974; Bame et al., 1977; Feldman et al., 1977, 1978; Gosling et al., 1978, 1981; Borrini et al., 1982]. Out of these studies has come the recognition that much of solar wind  $A(He)$  variability appears to be related to the large-scale structure of the interplanetary plasma (i.e., high speed streams, stream interfaces, transient disturbances, and sector structure).

In particular, flows with relative helium content considerably larger than the average value of 5% have been repeatedly associated with transient disturbances. Some early studies [e.g., Gosling et al., 1967; Bame et al., 1968; Lazarus and Binsack, 1969; Ogilvie et al., 1968; Hirshberg et al., 1971] suggested that anomalously high values of  $A(He)$  were found on occasion within a day or so following the passage of an interplanetary shock at 1 A.U. A later, more thorough, statistical study of 16 events where  $A(He)$  exceeded 0.15 established beyond doubt that high values of  $A(He)$  are preferentially (but not exclusively) associated with interplan-

etary shocks and large solar flares [Hirshberg et al., 1972a]. Further examples of large  $A(He)$  enhancements following shocks have been presented in recent years [e.g., Bame et al., 1979, 1981; Gosling et al., 1980]. In fact, about one half of all shocks observed at 1 A.U. are followed by  $A(He)$  enhancements  $\geq 0.8$  [Borrini et al., 1982]. On the other hand,  $A(He)$  enhancements need not be preceded by shocks; they are often observed in the low speed solar wind with no shock association [e.g., Fenimore, 1980]. Both with and without a shock association,  $A(He)$  enhancements often have unusually high ionization temperatures, indicative of an origin in active solar processes [Bame et al., 1979; Fenimore, 1980]. On at least one occasion, though, an  $A(He)$  enhancement had an unusually low ionization temperature [Gosling et al., 1980]. Collectively, these observations suggest that  $A(He)$  enhancements in the solar wind signal the arrival of plasma ejected from low in the corona during a disturbance such as a large solar flare or an eruptive prominence. It has been proposed that such plasma may be particularly rich in helium because of gravitational settling in the solar atmosphere [Hirshberg et al., 1970] or because of abnormal temperature, pressure, or density gradients associated with solar activity [Bame et al., 1977] or because of a runaway effect associated with large proton acceleration [Borrini and Noci, 1979].

Heretofore, with the exception of the work by Fenimore [1980], the emphasis of studies of  $A(He)$  enhancements has been on shock-related events. The purpose of the present work is a thorough analysis of large helium enhancements in the solar wind, with no restriction to shock-related events. Our study provides a firmer statistical basis for some earlier results and establishes several new associations for  $A(He)$  enhancements (hereinafter, following Fenimore, referred to as HAEs). The solar wind plasma data set used in our analysis has been collected by Los Alamos National Laboratory instruments about IMP 6-7-8 from 1971 through 1978. One hour averages have been employed. The instruments and data reduction procedures have been discussed in previ-

Copyright 1982 by the American Geophysical Union.

Paper number 2A0813.  
0148-0227/82/002A-0813\$5.00

ous publications [e.g., *Asbridge et al.*, 1976; *Feldman et al.*, 1976; *Bame et al.*, 1977], and the pertinent details for A(He) measurements are outlined in recent papers [e.g., *Borrini et al.*, 1981; *Gosling et al.*, 1981]. Magnetic field data has been obtained from the NSSDC [*King*, 1977, 1979] and solar radio data from the NOAA Solar Geophysical Data Book.

## 2. A STATISTICAL ANALYSIS OF HELIUM ABUNDANCE ENHANCEMENTS

A(He) measurements greater than the long-term average of 5% occur frequently, particularly in the low speed solar wind where A(He) is generally highly variable [e.g., *Bame et al.*, 1977; *Feldman et al.*, 1977]. For example, Figure 1 of *Borrini et al.* [1981] indicates that A(He) is greater than 0.07 approximately 10% of the time. To restrict our analysis to a manageable subset of the data and to eliminate variations that might not be related to the phenomenon we wish to discuss, we have chosen to study HAEs in which  $A(He) \geq 0.10$ . Examination of the above-mentioned figure reveals that such events encompass  $\sim 1\%$  of all hourly-averaged measurements. (Note that our choice is different from that used in several previous studies. *Hirshberg et al.* [1972a] chose to study events where  $A(He) \geq 0.15$ ; *Fenimore* [1980] studied events where  $A(He) \geq 0.09$ ; and *Borrini et al.* [1982] discussed post-shock events with  $A(He) \geq 0.08$ .) To be included in the present study, an event had to have  $A(He) \geq 0.10$  for at least 2 hours within a 24 hour interval. The starting time of the HAE was chosen to be the time of the first hourly averaged value in which  $A(He) \geq 0.10$ . If an event persisted for many hours, but with interruptions in which A(He) became less than 0.10 for periods less than 24 hours, the first starting time was kept and the event was considered a single HAE. In all, 73 HAE events were identified in this way; starting times for the events were tabulated in Table 1. We are confident that these 73 events encompass the entire range of large helium enhancements in the solar wind and can be used to characterize the major features of such events. Examination of Table 1 reveals that HAEs are prevalently isolated events, sometimes clustered in time, and very rarely recurrent. Also, the frequency of HAE observations is related to the solar cycle (i.e., it is high near solar maximum (1971, 1972, 1977, 1978) and low near solar minimum (1973–1976)).

Three examples of our selected HAE events are displayed in Figures 1–3. From top to bottom these figures show the solar wind A(He), proton density, bulk flow speed, and proton temperature for 6 day intervals approximately centered on each of three separate HAE events. One of these events, the HAE of May 22–23, 1978 (Figure 3) was preceded by  $\sim 1$  day by an observed shock at IMP, while the other two events (December 2, 1974, and May 2–4, 1977) occurred independent of either a shock or the sudden commencement of a geomagnetic storm. Although the HAE events of May 2–4, 1977 (Figure 2) and May 22–23, 1978 (Figure 3) have been treated as single events in our study, they have the appearance of multiple events. They may, in fact, have been produced by multiple solar activity outbursts. The abrupt rise in A(He) at the onset of the events in Figures 1–3 is a characteristic common to many HAEs. Finally, there is a clear tendency for the HAE events to occur at times of low proton temperatures, a correlation consistent with previous work [*Gosling et al.*, 1973; *Montgomery et al.*, 1974; *Bame et al.*, 1979].

Figure 4 presents the results of a superposed epoch analysis of the solar wind plasma and field data by using as key times the onsets of our 73 selected HAE events. The quantities plotted are A(He), proton density, bulk speed, alpha-proton speed difference, magnetic field strength, and proton temperature. A  $\pm 6$  day window about zero epoch has been chosen so as to allow an adequate assessment of the statistical significance of the results. The error bar plotted on the middle of the central line of each plot is the average variance of the parameter for the 12-day interval. The average A(He) profile is asymmetrical, rising rapidly (within  $\sim 4$  hours) to a peak of 0.17 at zero epoch, remaining above 0.10 for several hours, and then decaying slowly back to normal over a period of  $\sim 1.5$  days. This asymmetry may be an artifact of the way in which the data were superimposed; however, the asymmetry is consistent with our examination of individual events. In approximately half of the HAE events the initial rise in A(He) is abrupt and is followed by a gradual decay to average values over 1–2 days. Many other events consist of an isolated peak in A(He) lasting but a few hours. In addition, some of our HAE events are complex, such as illustrated in Figures 2 and 3, with the secondary enhancement beginning at a variable lag relative to the initial enhancement.

Neither the proton density nor the bulk flow speed show any pronounced average behavior in association with helium abundance enhancements. A very small maximum in proton density occurs  $\sim 0.5$  days before the maximum in A(He). This maximum, which is of marginal statistical significance, can be ascribed to interplanetary compression preceding the onset of helium enhancements. For instance, 44% of our HAEs follow (within 2 days) the passage of an interplanetary shock either observed directly or inferred from ground magnetograms (see Table 1). On the other hand, a density spike of possible coronal origin often is found at the leading edge of HAE events [*Bame et al.*, 1979].

A pronounced minimum in the average helium-proton speed difference is centered approximately on the maximum in average A(He). Previous studies have indicated that minimums in the speed difference are normally a result of enhanced Coulomb coupling between  $\text{He}^{++}$  and  $\text{H}^+$  in regions of high density and low temperature [Neugebauer, 1976]. Although the proton density is not enhanced at HAE crossing time, the proton temperature is depressed there, suggesting a possible Coulomb coupling enhancement. In fact, using the formulas in Neugebauer, one expects to observe a minimum in speed difference of the magnitude which is observed. However, the minimum may be the result of other processes. For example, magnetic confinement or an absence of wave deposition, or both, may account for the observed result.

A broad, and statistically significant, maximum in magnetic field strength coincides with the maximum in A(He). However, the field enhancement begins  $\sim 1$  day prior to the A(He) maximum and persists for  $\sim 2.5$  days thereafter. That is, the HAE events on the average occupy the core of regions of enhanced magnetic field strength. Although some of the field enhancement prior to the onset of the HAE may be the result of compression in interplanetary space, it is clear that the bulk of the field enhancement can not be explained in this way because the data show no evidence of compressive heating. Rather, a magnetic field enhancement is an intrinsic signal associated with HAE events. Examples

TABLE I. Helium Enhancements HAEs 1971/1978

Year	Month	Day	Hour	A(He) Maximum Value Observed Within the Event	Interplanetary Shock Association	Sudden Commencement Association	Radio Bursts Type II and/or IV Observed Ahead Within 5 Days	Radio Bursts Type II and/or IV Observed Within Days -2 to -4 Prior to HAE
1971	4	22	22	13.3		yes	yes	yes
1971	4	30	13	11.2		yes		
1971	5	17	18	24.5	yes	yes	yes	yes
1972	2	18	14	19.8			yes	yes
1972	2	26	17	12.3			yes	yes
1972	3	7	5*	13.1	yes	yes	yes	yes
1972	3	9	16*	23.4			yes	yes
1972	3	11	8*	11.5			yes	yes
1972	3	27	21	13.2			yes	yes
1972	4	13	22*	10.4			yes	yes
1972	4	16	4*	10.7				
1972	4	17	20*	11.5	yes			
1972	4	20	7*	12.5				
1972	4	21	13*	11.1	yes	yes		
1972	4	26	12*	13.1				
1972	4	29	5*	19.9				
1972	5	16	2	11.2	yes	yes	yes	yes
1972	6	21	20	14.5			yes	yes
1972	11	29	8	33.9			yes	yes
1973	1	19	1	11.0				
1973	1	20	18	14.8				
1973	2	18	18	11.8				
1973	4	13	17	16.1	yes	yes	yes	yes
1973	5	3	8*	15.1		yes	yes	yes
1973	5	5	1*	17.8			yes	yes
1973	5	21	13	12.6	yes	yes	yes	yes
1973	5	25	6	14.2			yes	yes
1973	9	13	7	11.6			yes	yes
1973	9	26	16	12.7			yes	yes
1974	1	25	0	10.8				
1974	2	22	12	10.8			yes	yes
1974	5	8	16	20.5			yes	yes
1974	6	10	22	11.5	yes	yes	yes	yes
1974	7	6	14	20.5	yes	yes	yes	yes
1974	7	31	16	11.7			yes	
1974	9	16	14	14.5	yes	yes	yes	yes
1974	10	13	15*	14.5	yes	yes	yes	yes
1974	10	15	23*	12.0		yes	yes	yes
1974	12	2	12	14.3			yes	yes
1975	1	6	11	12.0				
1975	3	7	16	22.4				
1976	5	3	8	13.3		yes	yes	yes
1976	12	18	21	21.25				
1977	2	14	16	16.0	yes		yes	
1977	5	2	21	19.5				
1977	5	29	16	11.0		yes		
1977	7	5	7	39.4				
1977	9	20	10*	11.3				
1977	9	22	19*	12.5	yes	yes	yes	yes
1977	9	27	7	10.7			yes	yes
1977	10	4	18	10.3		yes		
1977	10	21	2	40.2				
1977	10	27	23	21.6	yes	yes		
1977	11	5	6*	15.7				
1977	11	6	8*	11.1				
1977	12	15	6	12.4				yes
1978	1	5	17	19.9	yes	yes	yes	yes
1978	1	30	13	36.1	yes			
1978	3	5	6	13.9				
1978	4	10	23	29.2	yes	yes	yes	yes
1978	5	4	12	22.9			yes	yes
1978	5	8	11	16.3			yes	yes
1978	5	22	18	21.5	yes	yes	yes	yes
1978	5	31	15	18.2			yes	
1978	6	4	9	11.0	yes	yes	yes	yes
1978	7	5	18	16.3	yes	yes	yes	yes
1978	7	16	0*	21.2		yes	yes	yes
1978	7	18	11*	14.1			yes	yes
1978	9	8	15*	10.0		yes	yes	yes

TABLE I (continued)

Year	Month	Day	Hour	A(He) Maximum Value Observed Within the Event	Interplanetary Shock Association	Sudden Commencement Association	Radio Bursts Type II and/or IV Observed Ahead Within 5 Days	Radio Bursts Type II and/or IV Observed Within Days -2 to -4 Prior to HAE
1978	9	10	9*	12.7		yes	yes	yes
1978	9	30	5	37.4	yes	yes	yes	yes
1979	1	1	16*	13.5		yes	yes	yes
1979	1	3	13*	11.2		yes	yes	yes

\*Possible multiple event.

Note: The association with interplanetary shocks or sudden commencements refer to 48 hours prior to the event.

of noncompressive magnetic field enhancements have also been reported by *Burlaga and King* [1979] and *Klein and Burlaga* [1982].

Finally, a deep minimum in average proton temperature coincides with the HAE. This minimum is expected from our discussion of Figures 1-3 and from previous work. Although the temperature depression and the HAE overlap in Figure 4, an examination of individual events reveals occasions when they are spatially distinct. Because HAE events often exhibit anomalously hot ionization temperatures [Bame *et al.*, 1979; Fenimore, 1980], it is unlikely that the low proton temperature is of coronal origin. A more likely explanation is that these low temperatures result from enhanced cooling in interplanetary space [e.g., Gosling *et al.*, 1973; Montgomery

*et al.*, 1974] produced by either an adiabatic expansion within a closed magnetic field topology or a faster than normal expansion of the HAE plasma, or both.

Figure 5 shows the result of a superimposed epoch analysis of total pressure ( $P_T = \sum_i n_i k T_i + B^2/8\pi$ ), gas pressure ( $\sum_i n_i k T_i$ ) and magnetic pressure ( $B^2/8\pi$ ) where  $i = 1,3$  for electrons, protons, and alpha particles, respectively;  $k$  is Boltzman's constant; and  $B$  is the magnetic field strength) keying as in Figure 4 on onsets of our HAE events. A broad maximum in total pressure surrounds the onset time, although the maximum in A(He) coincides with what appears to be a local minimum in total pressure. The double peaked nature of the pressure profile results from having a high proton density and high field strength prior to the HAE, a

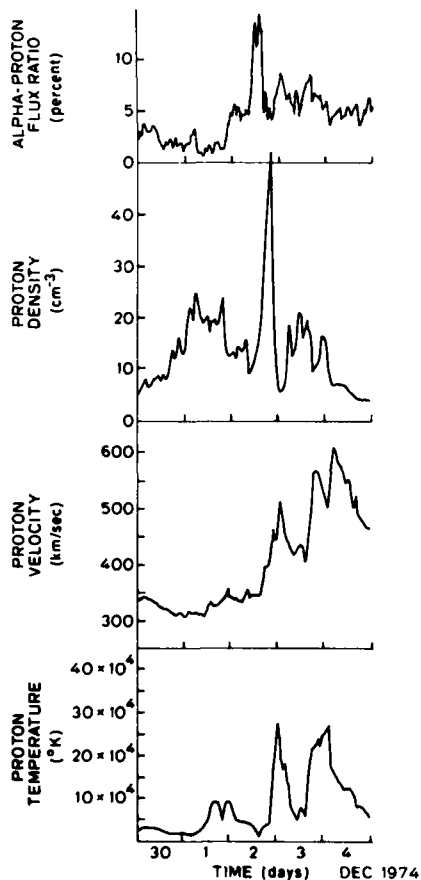


Fig. 1. One hour averaged solar wind data, November 30 to December 4, 1974. Notice the noncompressive density enhancement preceding the HAE.

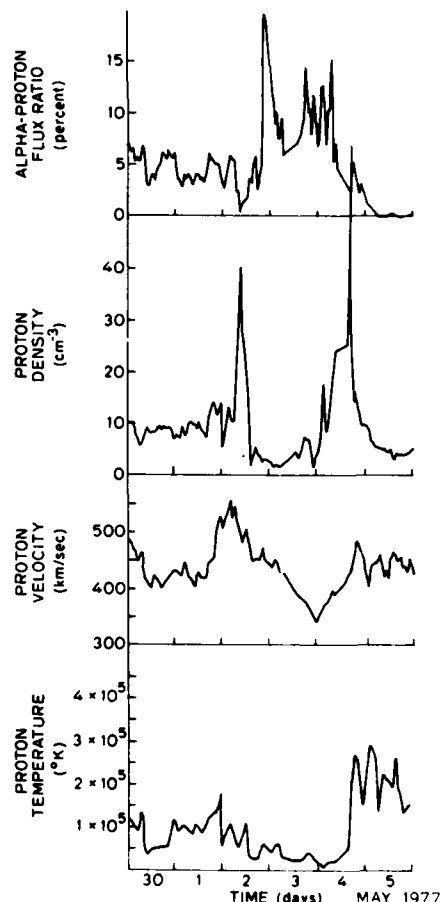


Fig. 2. One hour averaged solar wind data, April 30 to May 5, 1977. Notice the multi-peak structure of the helium enhancement and the contemporary proton temperature depression.

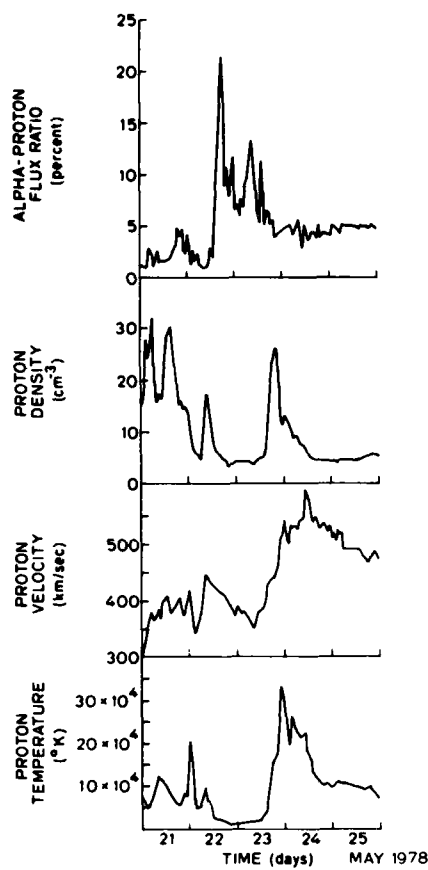


Fig. 3. One hour averaged solar wind data, May 20–25, 1978. An interplanetary shock was observed on May 21. Notice the multi-peak structure of the helium enhancement.

minimum in temperature coincident with the HAE, and an enhanced field strength in the decaying phase of the HAE. The overall pressure maximum associated with HAE events implies that, on the average, HAEs must be part of structures still dynamically evolving in interplanetary space.

Examination of Table 1 reveals that 33% of our HAE events are preceded or followed within  $\pm 3$  days by a companion HAE. In view of the fact that only 73 events have been identified in nearly 8 years of relatively continuous data coverage, this indicates that HAE events tend to occur in clusters. Furthermore, because of our definition of HAE events, the above percentage does not fully represent the phenomenon. Many examples of complex events such as displayed in Figures 2 and 3 are present in the data. Although such events are included in our study as single, they may in fact be multiple events. (On the other hand, this structuring may also be intrinsic to single HAE events [Bame et al., 1979]). A similar clustering tendency for interplanetary shocks has been reported previously [Borrini et al., 1982]. We believe that both multiple shocks and multiple HAE events are caused by multiple outbursts from the same solar activity center on a time scale of several days as reported, for example, by Hildner et al. [1976].

It is not obvious from an examination of individual HAEs that there is anything fundamentally different in the character of events associated with shock wave disturbances as opposed to those not so associated. To test this hypothesis, we repeated our superposed epoch analysis separating the events according to their association or lack of association with shock events (and sudden commencements). The only appreciable difference in the resulting profiles is that the flow speed is somewhat higher, on the average, at the onset of the HAE for the shock-associated events.

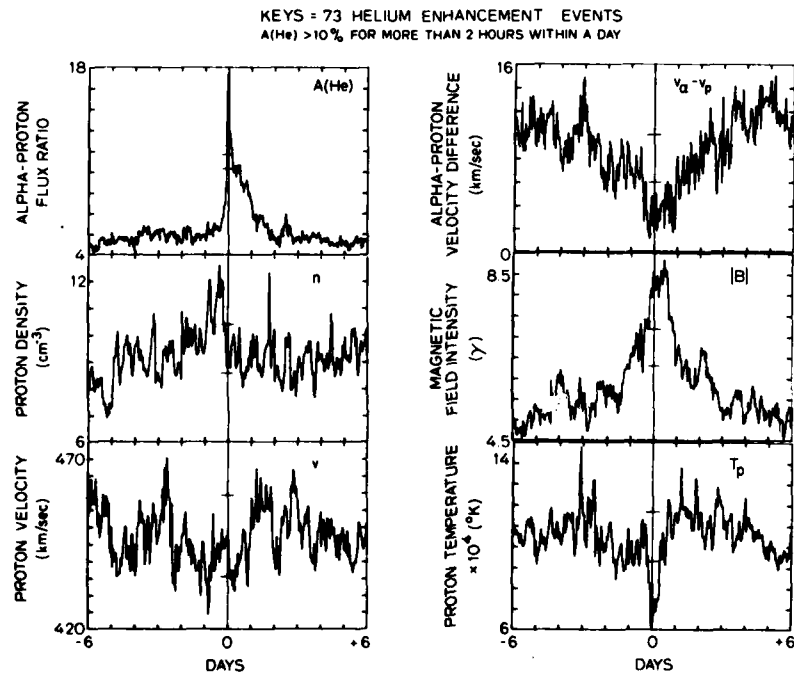


Fig. 4. Superposed epoch plots of solar wind alpha-proton flux ratio (helium abundance), proton density, bulk speed, alpha-proton velocity difference, magnetic field intensity, and proton temperature for 73 helium abundance enhancements at 1 A.U. (For lack of data only 42 keytimes are used in the magnetic field strength plot.) One hour averages of data are employed and the first hour with  $A(\text{He}) \geq 10\%$  is defined as the starting time of the enhancement.

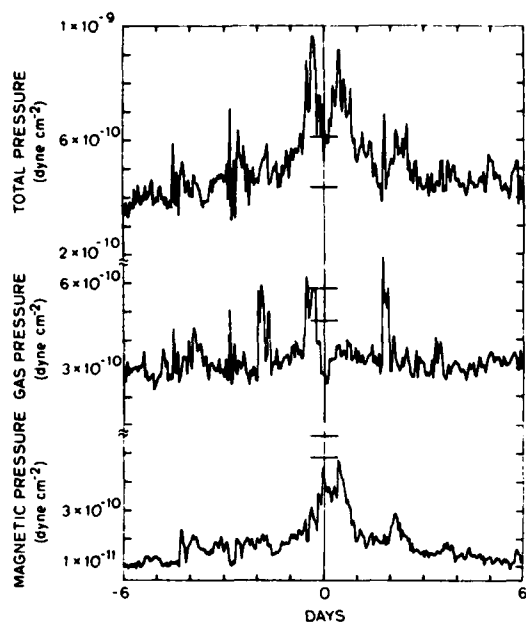


Fig. 5. Superposed epoch plots of solar wind total pressure, gas pressure, and magnetic pressure for the same key time set of 73 helium abundance enhancements of Figure 4. Again because of missing data, only 42 key times are used in the magnetic pressure plot, 69 in the gas pressure plot, and 40 in the total pressure plot.

### 3. THE ASSOCIATION OF HELIUM ABUNDANCE ENHANCEMENTS WITH TYPE II AND IV SOLAR RADIO BURSTS

As was already mentioned, approximately half of our HAE events follow within 2 days of a transient interplanetary shock-wave disturbance. Moreover, because there appears to be nothing fundamentally different between shock and non-shock associated HAE events, it is the authors' opinion that most, if not all, HAE events detected at 1 A.U. can be associated with the kind of transient mass ejection events so spectacularly photographed at the solar limbs by orbiting coronagraphs [e.g., *Stewart et al.*, 1974; *MacQueen et al.*, 1974]. However, few HAE events observed by earth-orbiting satellites would be expected to show a direct association with the limb events photographed by coronagraphs. To test for a definitive association of HAEs with coronal mass ejection events, we have studied the connection between HAE events and decametric type II and type IV solar radio bursts. Such bursts have been extensively studied by solar radio astronomers [see, for example, *Smerd and Dulk*, 1971; *Wild and Smerd*, 1972; *Stone*, 1974], are strongly correlated with large solar flares and eruptive prominences, and are believed to be manifestations of shock disturbances in the corona. Type II and IV bursts also have a very strong correlation with coronal mass ejection events; virtually all such bursts originating near the solar limb during the *Skylab* mission were accompanied by coronal mass ejections observed by the coronagraph [*Gosling et al.*, 1974; *Munro et al.*, 1979]. However, only 30% of all mass ejection events observed during this same period produced type II and/or IV radio bursts. In particular, it was the fastest ejections (observed speed  $>400$  km) that produced such bursts [*Gosling et al.*, 1976]. In summary, type II and/or IV

radio bursts are excellent indirect evidence of fast mass ejection events in the solar corona.

Using the reports of decametric type II and IV bursts of the Solar Geophysical Data Book distributed by NOAA, one finds that 68% of our HAE events are preceded within 5 days by a reported type II and/or type IV radio burst; 78% of the shock-associated HAE events fit in this category as well as 61% of the nonshock-associated events. If we restrict the interval of correlation to 2–4 days prior to the HAE event onset, 59% of our events are preceded by type II and/or IV radio bursts (72% of the shock-associated and 40% of the nonshock-associated events). These percentages, however, do not adequately reflect the degree of correlation between HAE events and type II and IV radio bursts because they say nothing about the average occurrence frequency of the radio bursts.

Figure 6 shows a plot of the total number of type II and IV radio bursts reported as a function of time relative to the observation of our 73 HAE events at 1 A.U. (day zero). The plot includes at least 4 lag days (days  $-12, -7, +1, +5$ ) sufficiently removed from the time of observation of the HAE events (day zero) as to allow an estimate of the random occurrence of type II and IV bursts in the corona. The number of random occurrences averaged over the above 4 lag days is 52, corresponding to a random occurrence rate of 0.71 per day. On the other hand, the average number of bursts reported 2–4 days prior to onset of the HAE events (where the distribution of bursts peaks) is 128, corresponding to an occurrence rate 2.5 times greater than random. A lag of 2–4 days is consistent with a reasonable range of average sun-earth transit speeds ( $435$ – $870$  km s $^{-1}$ ). However, not only is the distribution of bursts peaked at lags of 2–4 days, it is also greater than random at all lags from 0 to 6 days. This effect can almost certainly be attributed to the fact that radio bursts, like coronal mass ejection events, interplanetary shock disturbances, and HAE events, tend to cluster within intervals of several days.

Figures 7 and 8 show identical analyses for type IV and II

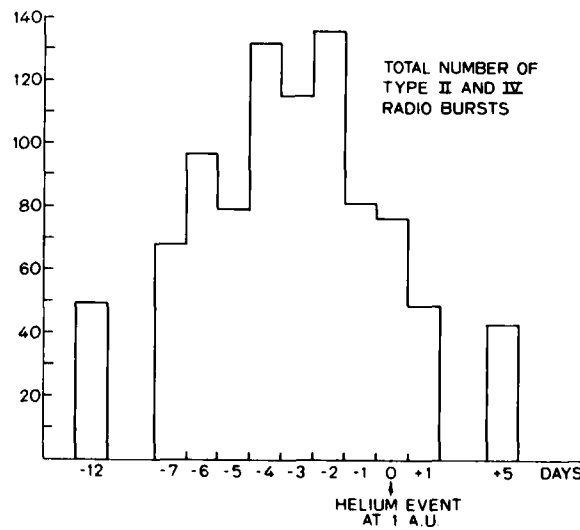


Fig. 6. A histogram of the total number of type II and IV decametric radio bursts observed on the sun as a function of time relative to the onset of a HAE event at 1 A.U. The peak of the distribution coincides with the time lag of 2–4 days (corresponding to an average sun-earth transit speed between 435 and 870 km/s).

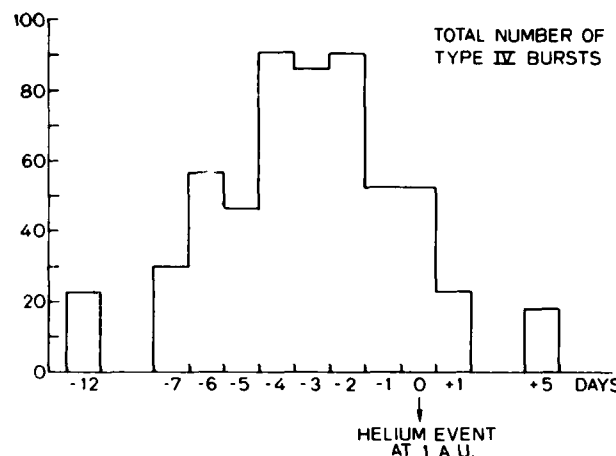


Fig. 7. Same as Figure 6 for the total number of type IV radio bursts only.

bursts considered separately. The same correlation is present for each individual set as for the combined set (Figure 6), but is considerably better for type IV bursts than for type II bursts, the peak signal to noise ratios being about 4.0 and 1.4, respectively. It is not presently clear why the correlation is better for type IV bursts since presumably both types of bursts are manifestations of fast outward-moving coronal mass ejection events.

The foregoing documents that a correlation exists between some HAE events and type II and IV solar radio bursts, and by inference fast-moving coronal mass ejection events. However, before leaving this topic, a few qualifications are in order. First, a fair fraction of the radio burst events included in our statistics and in Figures 6-8 are almost certainly limb events, which probably have little, if any, direct effect upon solar wind conditions near the earth. Thus, for example, our statement that 59% of all HAE events are preceded 2-4 days earlier by one or more type II and/or type IV bursts almost certainly overestimates the percentage of HAE events which actually are directly associated with coronal transients that produced such radio bursts. Second, we have not established a one-to-one correlation between HAE events and either type II and/or IV radio bursts or fast coronal mass ejection events. Nor is there any good reason to expect that a one-to-one correlation should in fact exist. Rather, we expect that HAE events in the solar wind at 1 AU are a signature (and not necessarily the only one or an invariant one) of coronal mass ejection events pretty much independent of the speed of the ejection event (see also Ogilvie and Hirshberg, 1974). The very fast ejection events that produce type II and/or IV radio bursts are a special subset of such events. It is important to document, as has been done here, that this special subset of mass ejection events has a strong, positive correlation with HAE events at 1 AU because it makes plausible the inference that all HAE events are caused by transient processes in the solar atmosphere.

#### 4. OBSERVATIONAL SUMMARY

In the previous sections we presented several observations supporting the association between HAEs at 1 AU and transient mass ejections in the corona. These observations are summarized briefly below:

1. Helium enhancements are sporadic phenomena, sometimes clustered in time, very rarely recurrent.
2. The occurrence frequency of HAEs is related to the solar cycle (frequent at maximum, scarce at minimum).
3. The HAE events defined in section 2 are associated with interplanetary shocks in 44% of the cases.
4. The plasma pattern associated with HAEs is independent of shock occurrence.
5. This plasma pattern features high magnetic field strength, low proton temperature, low alpha-proton velocity difference, and high total pressure.
6. Helium enhancements at 1 AU are often associated with type II and IV radio bursts in the corona.

#### 5. DISCUSSION

Large enhancements in the relative abundance of helium in the solar wind occur relatively infrequently. This paper has concentrated on enhancements wherein  $A(\text{He})$  achieved values greater than 0.10, accounting for  $\sim 1\%$  of all hourly averaged measurements in the 1971-1978 interval. Increases in  $A(\text{He})$  of this magnitude were identified in 73 separate events, only about half of which were preceded within 2 days by an observed shock or sudden commencement of a geomagnetic storm. Said another way, a substantial fraction of solar wind helium abundance enhancements occur in the absence of any shock wave disturbance. These enhancements, though, do not seem to differ in any substantial way from the shock related ones; in particular both types of enhancements are associated with very similar plasma characteristics.

A superposed epoch analysis of plasma and field data has been performed to determine the average character of  $A(\text{He})$  enhanced plasma. Typically, these enhancements occur within plasma of average particle density and flow speed, but unusually low proton temperature and high magnetic field strength. Whereas on the average the abundance enhancement coincides spatially with the region of anomalously low temperature, the region of high field strength is considerably broader than the abundance enhancement. There is little evidence of a density compression or heating, which might suggest that the field enhancement is produced by dynamical processes in interplanetary space. We thus interpret the high field measurement to mean that helium abundance enhancements originate in coronal regions of unusually high field strength. On the other hand, we interpret the low temperatures to be evidence that these magnetic structures are either topologically closed (hence adiabatically cooling) or have expanded considerably faster than normal in transit from the sun. Further possible evidence for a closed structure sur-

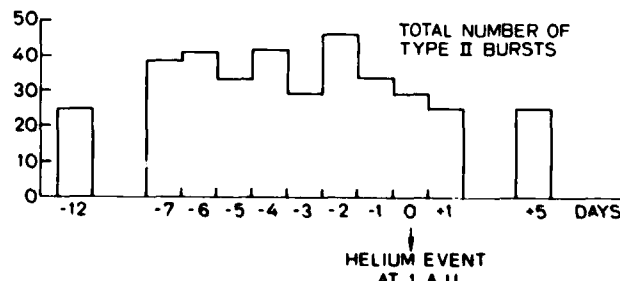


Fig. 8. Same as Figure 6 for the total number of type II radio bursts only.

rounding the helium rich plasma is the observation of low average alpha-proton velocity difference within HAEs. A magnetic confinement could help to create a region in which the process responsible for the preferential acceleration of alpha particles is not effective, although this explanation is not necessary [see, e.g., Neugebauer, 1976].

We have presented evidence that suggests (but does not prove) that HAEs are a 1 A.U. signal of coronal transients. Because the typical coronal mass ejection event has a speed at four solar radii ( $\sim 470 \text{ km s}^{-1}$ ) [Gosling et al., 1976], which is not far different from the average solar wind speed at 1 A.U. ( $\sim 450 \text{ km s}^{-1}$ ), we should not be surprised that helium abundance enhancements typically occur within plasma of only average speed. By way of contrast, one of the characteristics that distinguishes coronal mass ejection events in the corona is their higher than average density. The fact that these events seem to have only average density at 1 A.U. suggests that they expand in transit from the sun to a greater degree than does the ordinary solar wind stream tube. This suggestion is consistent with the observation that abundance enhancements typically are also regions of high pressure (but low proton temperature) still evolving dynamically even at 1 A.U.

It is unlikely that helium abundance enhancements wherein  $A(\text{He}) \geq 0.10$  account for all coronal mass ejection events in the solar wind at 1 A.U., since these enhancements occur much less frequently than do coronal mass-ejection events that occur somewhere on the sun at a rate of about 1 per day, depending on the phase of the solar cycle [Hildner et al., 1976]. What, then, is the 1 A.U. signature of these other mass ejection events, and why should the signature vary? One possibility is that a subset of abundance enhancements with  $0.05 \leq A(\text{He}) \leq 0.10$  also signal mass ejection events at 1 A.U. Another possibility is that a subset of so-called 'noncompressive density enhancements' [Gosling et al., 1977] are such a signal [e.g., Fenimore, 1980]. (On the other hand, a large fraction of noncompressive density enhancements have anomalously low  $A(\text{He})$  and almost certainly signal spacecraft intersections with coronal streamers [Borrini et al., 1981; Gosling et al., 1981]. And, finally, it is possible that magnetic 'clouds' [e.g., Burlaga and Behannon, 1982] without  $A(\text{He})$  enhancements form a subset of coronal mass ejection events at 1 A.U. The great variety of physical appearances of mass ejection events in the corona [see, for example, the discussion by Munro et al., 1979] suggests that the physical structure of these events may vary considerably from one event to the next. Altogether, then, there is no reason to expect that a single anomaly such as an  $A(\text{He})$  enhancement would be sufficient to identify all coronal mass ejections in the solar wind. On the other hand, on the basis of previous and our present findings, we feel confident that major helium enhancements are one of the clearest indications of transient mass ejections at 1 A.U.

**Acknowledgments.** G. Borrini would like to acknowledge the Stanford University Solar-Terrestrial Physics Group for the very kind hospitality she has enjoyed as a visitor there. In particular, she thanks J. M. Wilcox and P. H. Scherrer for valuable discussions during the progress of this work, Debbie Blaskowski for the typing of the manuscript, and Willelm Terluin for the drafting of figures. The work at Stanford University has been supported by a fellowship grant from the European Space Agency and in part by the Office of Naval Research under contract N00014-77-C-2207, by the National Aeronautics and Space Administration under grant NGR 05-020-559, and contract NASS-24420, by the Division of Atmospheric

Sciences, Solar Terrestrial Research program of the National Science Foundation under grant ATM80-20421, and by the Max C. Fleischmann Foundation. The Los Alamos solar wind data were obtained from the IMP program of the U.S. National Aeronautics and Space Administration (NASA). Work at Los Alamos was performed under the auspices of the U.S. Department of Energy and was supported in part by NASA.

The editor thanks M. Neugebauer and another referee for their assistance in evaluating this paper.

## REFERENCES

Asbridge, J. R., S. J. Bame, W. C. Feldman, and M. D. Montgomery, Helium and hydrogen velocity differences in the solar wind, *J. Geophys. Res.*, 81, 2719, 1976.

Bame, S. J., J. R. Asbridge, A. J. Hundhausen, and I. B. Strong, Solar wind and magnetosheath observations during the January 13-14, 1967 geomagnetic storm, *J. Geophys. Res.*, 73, 5761, 1968.

Bame, S. J., Spacecraft observations of the solar wind composition, *Solar Wind, NASA Spec. Publ. SP-308*, 1972.

Bame, S. J., J. R. Asbridge, W. C. Feldman, and J. T. Gosling, Evidence for a structure free state at high solar wind speeds, *J. Geophys. Res.*, 82, 1487, 1977.

Bame, S. J., J. R. Asbridge, W. C. Feldman, E. E. Fenimore, and J. T. Gosling, Solar wind heavy ions from flare-heated coronal plasma, *Solar Phys.*, 62, 179, 1979.

Bame, S. J., J. R. Asbridge, W. C. Feldman, J. T. Gosling and R. D. Zwickl, Bi-directional streaming of solar wind electrons  $>80 \text{ eV}$ : ISEE evidence for a closed-field structure within the driver gas of an interplanetary shock, *Geophys. Res. Lett.*, 8, 173, 1981.

Bollea, D., V. Formisano, P. C. Hedgecock, G. Moreno, and F. Palmiotti, Heos 1 helium observations in the solar wind, in *Solar Wind, NASA Spec. Publ. SP-308*, 1972.

Borrini, G., and G. Noci, Dynamics and abundance of ions in coronal holes, *Solar Phys.*, 64, 367, 1979.

Borrini, G., J. T. Gosling, S. J. Bame, W. C. Feldman, and J. M. Wilcox, Solar wind helium and hydrogen structure near the heliospheric current sheet: A signal of coronal streamers at 1 A.U., *J. Geophys. Res.*, 86, 4565, 1981.

Borrini, G., J. T. Gosling, S. J. Bame, and W. C. Feldman, An analysis of shock wave disturbances observed at 1 A.U. from 1971 through 1978, *J. Geophys. Res.*, 87, 4365, 1982.

Burlaga, L. F., and J. H. King, Intense interplanetary magnetic fields observed by geocentric spacecraft during 1963-1975, *J. Geophys. Res.*, 84, 6633, 1979.

Burlaga, L. F., and K. W. Behannon, Magnetic clouds between 2-4 AU: Voyager observations, in press, *Solar Phys.*, 1982.

Feldman, W. C., J. R. Asbridge, S. J. Bame, and J. T. Gosling, High-speed solar wind flow parameters at 1 AU, *J. Geophys. Res.*, 81, 5054, 1976.

Feldman, W. C., J. R. Asbridge, S. J. Bame, and J. T. Gosling, Plasma and magnetic fields from the sun, in *The Solar Output and Its Variation*, edited by O. R. White, p. 251, Colorado Associated University Press, Boulder, 1977.

Feldman, W. C., J. R. Asbridge, S. J. Bame, and J. T. Gosling, Long-term variations of selected solar wind properties: IMP 6, 7, and 8 results, *J. Geophys. Res.*, 83, 2177, 1978.

Fenimore, E. E., Solar wind flows associated with hot heavy ions, *Astrophys. J.*, 235, 245, 1980.

Geiss, J., P. Hirt, and H. Leutwyler, On acceleration and ions in corona and solar wind, *Solar Phys.*, 12, 458, 1970.

Gosling, J. T., J. R. Asbridge, S. J. Bame, A. J. Hundhausen, and I. B. Strong, Measurements of the interplanetary solar wind during the large geomagnetic storm of April 17-18, 1965, *J. Geophys. Res.*, 72, 1813, 1967.

Gosling, J. T., V. Pizzo, and S. J. Bame, Anomalously low proton temperatures in the solar wind following interplanetary shock waves: Evidence for magnetic bottles?, *J. Geophys. Res.*, 78, 2001, 1973.

Gosling, J. T., E. Hildner, R. M. MacQueen, R. H. Munro, A. I. Poland, and C. L. Ross, Mass ejections from the sun: A view from Skylab, *J. Geophys. Res.*, 79, 4581, 1974.

Gosling, J. T., E. Hildner, R. M. MacQueen, R. H. Munro, A. I. Poland, and C. L. Ross, The speeds of coronal mass ejection events, *Solar Phys.*, 48, 389, 1976.

Gosling, J. T., E. Hildner, J. R. Asbridge, S. J. Bame, and W. C.

Feldman, Noncompressive density enhancements in the solar wind, *J. Geophys. Res.*, **82**, 5005, 1977.

Gosling, J. T., J. R. Asbridge, S. J. Bame, and W. C. Feldman, Solar wind stream interfaces, *J. Geophys. Res.*, **83**, 1401, 1978.

Gosling, J. T., J. R. Asbridge, S. J. Bame, W. C. Feldman, and R. D. Zwickl, Observations of large fluxes of  $\text{He}^+$  in the solar wind following an interplanetary shock, *J. Geophys. Res.*, **85**, 3431, 1980.

Gosling, J. T., G. Borrini, J. R. Asbridge, S. J. Bame, W. C. Feldman, and R. T. Hansen, Coronal streamers in the solar wind at 1 A.U., *J. Geophys. Res.*, **86**, 5438, 1981.

Hildner, E., J. T. Gosling, R. M. MacQueen, R. H. Munro, A. I. Poland, and C. L. Ross, Frequency of coronal transients and solar activity, *Solar Phys.*, **48**, 127, 1976.

Hirshberg, J., A. Alksne, D. S. Colburn, S. J. Bame, and A. J. Hundhausen, Observations of a solar flare induced interplanetary shock and helium-enriched driver gas, *J. Geophys. Res.*, **75**, 1, 1970.

Hirshberg, J., J. R. Asbridge, and D. E. Robbins, The helium-enriched interplanetary plasma from the proton flares of August/September 1966, *Solar Phys.*, **18**, 313, 1971.

Hirshberg, J., S. J. Bame, and D. E. Robbins, Solar flares and solar wind helium enrichments: July 1965-July 1967, *Solar Phys.*, **23**, 467, 1972a.

Hirshberg, J., J. R. Asbridge, and D. E. Robbins, Velocity and flux dependence of the solar wind helium abundance, *J. Geophys. Res.*, **77**, 3583, 1972b.

Hirshberg, J., J. R. Asbridge, and D. E. Robbins, The helium component of solar wind velocity streams, *J. Geophys. Res.*, **79**, 934, 1974.

Hollweg, J. V., and J. M. Turner, Acceleration of solar wind  $\text{He}^{++}$ , 3, Effects of resonant and nonresonant interactions with transverse waves, *J. Geophys. Res.*, **83**, 97, 1978.

Hollweg, J. V., Minor ions in the low corona, *J. Geophys. Res.*, **86**, 8899, 1981.

Jokipii, J. R., Effects of diffusion on the composition of the solar corona and the solar wind, in *The Solar Wind*, edited by R. J. Mackin and M. Neugebauer, p. 215. Pergamon, New York, 1966.

Joselyn, J. A., and T. E. Holzer, A steady three-fluid coronal expansion for nonspherical geometries, *J. Geophys. Res.*, **83**, 1019, 1978.

King, J. H., *Interplanetary Medium Data Book*, Rep. NSSDC 7704, NASA Goddard Space Flight Center, Greenbelt, Md., 1977.

King, J. H., *Interplanetary Medium Data Book* (Suppl. 1), Rep. NSSDC 7908, NASA Goddard Space Flight Center, Greenbelt, Md., 1979.

Klein, L., and L. F. Burlaga, Interplanetary magnetic clouds at 1 A.U., **87**, 613, *J. Geophys. Res.*, 1982.

Kopp, R. A., G. Borrini, G. Noci, and J. Brackbill, Magnetic reconnection in coronal streamers, *Eos Trans. AGU*, **62**, 376, 1981.

Lazarus, A. J., and J. H. Binsack, Observations of the interplanetary plasma subsequent to the July 7, 1966 proton flare, *Ann. I.Q.S.Y.*, **3**, 378, 1969.

MacQueen, R. M., J. A. Eddy, J. T. Gosling, E. Hildner, R. H. Munro, G. A. Newkirk, A. I. Poland, and C. L. Ross, The outer solar corona as observed from Skylab: preliminary results, *Astrophys. J.*, **187**, L85, 1974.

Montgomery, M. D., J. R. Asbridge, S. J. Bame, and W. C. Feldman, Solar wind electron temperature depressions following some interplanetary shock waves: Evidence for magnetic merging?, *J. Geophys. Res.*, **79**, 3103, 1974.

Moreno, G., and F. Palmiotti, Variations of  $\alpha$ -particle abundance in the solar wind, *Solar Phys.*, **30**, 207, 1973.

Munro, R. H., J. T. Gosling, E. Hildner, R. M. MacQueen, A. I. Poland, and C. L. Ross, The association of coronal mass ejection transients with other forms of solar activity, *Solar Phys.*, **61**, 201, 1979.

Nakada, M. P., A study of the composition of the lower solar corona, *Solar Phys.*, **7**, 302, 1969.

Neugebauer, M., and C. W. Snyder, Mariner 2 observations of the solar wind, I. Average properties, *J. Geophys. Res.*, **71**, 4469, 1966.

Neugebauer, M., The role of Coulomb collisions in limiting differential flow and temperature differences in the solar wind, *J. Geophys. Res.*, **81**, 78, 1976.

Neugebauer, M., Observations of solar-wind helium, *Fund. Cosmic Phys.*, **7**, 131, 1981.

Ogilvie, K. W., L. F. Burlaga, and T. D. Wilkerson, Plasma observations on Explorer 34, *J. Geophys. Res.*, **73**, 6809, 1968.

Ogilvie, K. W., and T. D. Wilkerson, Helium abundance in the solar wind, *Solar Phys.*, **8**, 435, 1969.

Ogilvie, K. W., Helium abundance variations, *J. Geophys. Res.*, **77**, 4227, 1972.

Ogilvie, K. W., and J. Hirshberg, The solar cycle variation of the solar wind helium abundance, *J. Geophys. Res.*, **79**, 4595, 1974.

Robbins, D. E., A. J. Hundhausen, and S. J. Bame, Helium in the solar wind, *J. Geophys. Res.*, **75**, 1178, 1970.

Smerd, S. F., and G. A. Dulk, 80 MHZ radioheliograph evidence on moving type IV bursts and coronal magnetic fields, in *Solar Magnetic Fields*, edited by R. Howard, D. Reidel, Hingham, Mass., 1971.

Stewart, R. T., M. K. McCabe, M. J. Koomen, R. T. Hansen, and G. Dulk, Observations of coronal disturbances from 1 to 9 R, *Solar Phys.*, **36**, 203, 1974.

Stone, R. G., Travelling solar radio bursts, in *Solar Wind Three*, edited by C. T. Russell, University of California, Los Angeles, 1974.

Wild, J. P., and S. F. Smerd, Radio bursts from the solar corona, *Ann. Rev. Astron. Astrophys.*, **10**, 159, 1972.

(Received March 9, 1982;  
revised May 10, 1982;  
accepted May 21, 1982.)

2-8  
DT